Mineralogical and geochemical characterization of the Riópar non-sulfide Zn-(Fe-Pb) deposits (Prebetic Zone, SE Spain)

Dídac Navarro-Ciurana[1*], Luis Alberto Campos-Quispe[1], Esteve Cardellach[1], Elena Vindel[2], David Gómez-Gras[1], Albert Griera[1], Mercè Corbella[1]

[1]Departament de Geologia, Facultat de Ciències, Universitat Autònoma de Barcelona, Edifici Cs s/n, 08193 Bellaterra (Cerdanyola del Vallès), Spain

[2]Departamento de Cristalografía y Mineralogía, Facultad de Ciencias Geológicas, Universidad Complutense de Madrid, c/ José Antonio Novais s/n, 28040, Madrid, Spain

*Corresponding author (e-mail: didac.navarro.ciurana@gmail.com)

ABSTRACT: The present paper reports the first detailed petrological and geochemical study of non-sulfide Zn-(Fe-Pb) deposits in the Riópar area (Prebetic Zone of the Mesozoic Betic Basin, SE Spain), constraining the origin and evolution of ore-forming fluids. In Riópar both sulfide and non-sulfide Zn-(Fe-Pb) ("calamine") ores are hosted in hydrothermally dolomitized Lower Cretaceous limestones. The hypogene sulfides comprise sphalerite, marcasite and minor galena. Calamine ores consist of Zn-carbonates (smithsonite and scarce hydrozincite), associated with abundant Fe-(hydr)oxides (goethite and hematite) and minor Pb-carbonates (cerussite). Three smithsonite types have been recognized: i) Sm-I consists of brown anhedral microcrystalline aggregates as encrustations replacing sphalerite; ii) Sm-II refers to brownish subhedral aggregates of rugged appearance related with Fe oxi-hydroxides in the surface crystals, which replace extensively sphalerite; and iii) Sm-III smithsonite appears as coarse grayish botryoidal aggregates in microkarstic cavities and porosity.

Hydrozincite is scarce and appears as milky white botryoidal encrustations in cavities replacing smithsonite. Also, two types of cerussite have been identified: i) Cer-I cerussite consists of fine crystals replacing galena along cleavage planes and crystal surfaces; and ii) Cer-II conforms fine botryoidal crystals found infill porosity. Calcite and thin gypsum encrustations were also recognized. The field and petrographic observations of the Riópar non-sulfide Zn-(Fe-Pb) revealed two successive stages of supergene ore formation under meteoric fluid processes: i) "gossan" and "red calamine" formation in the uppermost parts of the ore with deposition of Fe-(hydr)oxides and Zn- and Pb-carbonates (Sm-I, Sm-II and Cer-I), occurring as direct replacements of Zn-Pb sulfides; and ii) "gray calamine" ore formation with deposition of Sm-III, Cer-II and hydrozincite infilling microkarst cavities and porosity. The stable isotope variation of Riópar smithsonite is very similar to those obtained in other calamine-ore deposits around the world. Their C-O isotope data ($\delta^{18}O$: +27.8 to +29.6‰ V-SMOW; $\delta^{13}C$: -6.3 to +0.4‰ V-PDB), puts constrains on: i) the oxidizing fluid type, which was of meteoric origin with temperatures of 12 to 19ºC, suggesting a supergene weathering process for the calamine-ore formation under a temperate climate; and ii) the carbon source, that resulted from mixing between two CO_2 components derived from: the dissolution of host-dolomite (^{13}C-enriched source) and vegetation decomposition (^{13}C-depleted component).

KEYWORDS: Non-sulfide Zn ores; Calamine; Supergene; MVT; Riópar; Southeast Spain

1 Introduction

Until the beginning of the 20th century, zinc metal was extracted from non-sulfide ore (e.g., Boni and Mondillo et al., 2015). Zn ores shifted towards sphalerite when flotation processes were optimized, allowing a more efficient recovery. Nevertheless, recent improvement in hydrometallurgical solvent-extraction and electro-winning techniques for the treatment of non-sulfide zinc ores paves the way for a renewal of economic interest for this mineralization-type throughout the world (Cole and Sole, 2002; Gnoinski, 2007; Hosseini, 2008), as it reduces costs and environmental pollution. This is reflected in the number of scientific papers published in recent years which focus on such ore from various countries (e.g., Belgium: Coppola et al., 2008; Sardinia: Boni et al., 2003; Irish Midlands: Balassone et al., 2008; Morocco: Choulet et al., 2014; Iran: Daliran et al., 2013; Yemen: Mondillo et al., 2014; Turkey; Santoro et al., 2013; Kazakhstan: Boland et al., 2003; Namibia: Borg et al., 2003; Australia: Groves et al., 2003; Peru: Boni et al., 2009a; Brazil: Monteiro et al., 2007).

Non-sulfide zinc ore is also known as “calamine”, which is a convenient field term used by mine geologists to designate a mixture of Zn minerals. Usually, calamine ore is accompanied by non-sulfide Pb and Fe specimens. Historically, the term “calamine” included Zn-carbonates (e.g., smithsonite, hydrozincite), Zn-silicates (e.g., willemite, hemimorphite), Zn-oxides (e.g., zincite, franklinite, gahnite), Zn-phosphates (e.g., tarbuttite, scholzite,) and Zn-rich clays (e.g., sauconite, fraipontite) (as listed in Hitzman et al., 2003). Locally, non-sulfide Zn minerals may be associated with Pb-carbonates (e.g., cerussite, hydrocerussite), Pb-sulfates (e.g., anglesite), Fe-carbonates (e.g., siderite) and Fe-(hydr)oxides (e.g., goethite, hematites) among others (Boni and Large, 2003; Coppola et al., 2008). Numerous authors classified the non-sulfide zinc deposits as hypogene and supergene according to their mineralogy, geological characteristics and genetic setting (e.g., Heyl and Boizon, 1962; Hitzman et al., 2003).

The hypogene non-sulfide Zn deposits, related to warm fluids, usually contain willemite, zincite and franklinite, whereas supergene non-sulfide zinc deposits, caused by the oxidation of primary Zn-sulfide ores, are commonly associated with smithsonite, hydrozincite and hemimorphite. Furthermore, Boni et al. (2007) suggest a hypogene formation of Zn-carbonate ores in the Angouran deposit (NW Iran). The supergene type may be subdivided in three groups (Boni and Mondillo, 2015; Heyl and Boizon, 1962; Hitzman et al., 2003; Reichert and Borg, 2008): i) replacement of hypogene Zn-sulfides, traditionally called "red calamine" ore, with >20% Zn, >7% Fe and variable amounts of Pb or Ag; ii) wall-rock replacements or "white calamine" ore, which typically contain <40% Zn, <7% Fe and very low concentrations of Pb, resulting from zinc migration and redeposition by host-carbonate replacement; and iii) residual accumulation and karst- and microkarst-fill deposits, called "gray calamine" ore according to Choulet et al. (2014), which emerge from zinc concentration in karst cavities, sinkholes and porosities.

The most important non-sulfide zinc concentrations in Spain are represented by supergene calamine deposits related to primary sulfide mineralization (Fig. 1). The Basque-Cantabrian (N Spain) and Maestrat basins (E Spain) contain calamines associated with Zn-Pb Mississippi Valley-type (MVT) deposits (Grandia et al., 2003a, 2003b; Velasco et al., 1994) hosted in Cretaceous sequences. The Reocín deposit (Basque-Cantabrian basin), one of the largest Zn ore systems in Europe, consists of Zn and Fe sulfides with an estimated production history of about 3.76 Mt calamine ore (Boni and Large, 2003). Lanestosa, Coto Txomin and Matienzo mines located within the same basin, comprise a resource of mixed oxide and sulfide estimated at 3 Mt at 11% Zn (Grandia et al., 2003a). In the Maestrat basin, the estimated resource of mixed oxide and sulfide at Resurrección mine was 30,000 t at 6.7% Zn (Grandia et al., 2003b).

The oldest working brass factory of the Iberian Peninsula is located at Riópar (Albacete, SE Spain), in the northern part of the Betic Cordillera. The foundries opened in 1773 utilizing the Zn from the calamine of nearby mines. These deposits are rather small (~20,000 t extracted Zn: Navarro-Ciurana et al., 2015b) and are hosted in dolomitized rocks of Lower Cretaceous age. They are spatially associated with the supergene alteration of MVT mineralization and have not been studied in detail so far. Therefore, the main goals of the present contribution are: i) to describe the occurrence, setting, distribution and geometry of the Riópar non-sulfide Zn-(Fe-Pb) ores; ii) to use mineralogical and geochemical data to constrain the origin and evolution of the ore-forming fluids; and iii) to develop a conceptual model for the genesis of the calamine mineralization.

2 Regional geological setting and Betic Zn-Pb ores

The studied area is located in the Prebetic Zone of the External part of the Betic Cordillera (SE Spain). It forms the westernmost component of the Mediterranean Alpine chain, together with the Rif, in northern Morocco, and the Tell-Kabylies Ranges, in northern Algeria (e.g., Vera et al., 2004). The Betic cordillera is divided into three structural and tectonosedimentary units (Fig. 1) (e.g., Fallot, 1948): i) the External Zones, which comprise the Prebetic and Subbetic Zones, consists of Triassic to Paleogene marine sedimentary rocks generally unaffected by Alpine metamorphism; ii) the Internal Zones, with the Malaguide, Alpugárride and Nevado-Filabride complexes, variably metamorphosed nappes, constituting the most deformed part of the orogen; and iii) the Campo de Gibraltar Complex, which is characterized by Cretaceous to Cenozoic sediments deposited in a deep-water flysch basin between the Internal and External

Betics. The Betic Chain is characterized by an abundance of varied mineral deposits (e.g., Fe, Pb, Zn, Ag, Au) which gives it a potential mining interest (e.g. Sánchez-Valverde et al., 2013).

2.1 The Prebetic Zone

The Prebetic Zone, a broad Alpine tectonic unit that corresponds to the outer portion of the foreland NNW-verging fold-and-thrust belt of the Betic Cordillera (García-Hernández et al., 1980), consists of a Mesozoic to Cenozoic carbonate and clastic rocks sequence of up to 2000 m thick, that was originally deposited on the southern Iberian continental paleomargin (Vera et al., 2004). The Prebetic Zone became detached from the Hercynian basement along Upper Triassic sediments during the main Alpine orogenic stage (Barbero and López-Garrido, 2006). It is traditionally subdivided into two main zones (Fig. 1) on the basis of tectonostratigraphic criteria (Barbero and López-Garrido, 2006; García-Hernández et al., 1980; Vera et al., 2004). The External Prebetic area, dominated by shallow internal platform facies, corresponds to the deformed part of the northern basin with frequent stratigraphic gaps and extensive exposures of Triassic and Jurassic rocks and scarce Cretaceous sediments. The Internal Prebetic zone, dominated by marginal platform to slope facies, consists of large folds and thrusts structures with absence of Triassic, scarcity of Jurassic and extensively exposed Cretaceous and Paleogene sediments.

The sedimentation of the region during the Mesozoic and Cenozoic was controlled by various successive tectonic stages (Banks and Warburton, 1991; Barbero and López-Garrido, 2006; Calvo et al., 1978; García-Hernández et al., 1980; Montenat et al., 1996; Pedrera et al., 2014; Vergés and Fernàndez, 2012; Vilas et al., 2001). The first episode consisted of a Triassic rifting, caused by the Tethys Ocean opening and the

Pangea breakup that marks the initial divergence between the European and African plates. A second, post-rifting stage occurred during Early to Middle Jurassic, it is characterized by the development of shallow carbonate platforms within a thermal subsidence context. Another rifting episode occurred from the Late Jurassic to the Early Cretaceous periods, related to the North Atlantic Ocean opening, which led to the formation of the Prebetic and Subbetic basins and a large number of tectonic grabens. The Late Cretaceous post-rifting stage was characterized by little tectonism and the development of extensive marine carbonate platforms. A fourth tectonic episode consisted of a compressive/transpresive stage that began in the Late Cretaceous (late Santonian: Vergés and Fernàndez, 2012) and continued during Paleogene times; it was due to the convergence of the African and Iberian plates. Finally, a Miocene collision event structured the Prebetic Zone and allowed the development of Lower to Middle Miocene transgressive marine sin-orogenic deposits, which pass upwards into Upper Miocene continental post-orogenic sedimentation (Calvo et al., 1978). From late Miocene (Tortonian: Braga et al., 2003) to the present, the combined effect of regional uplift, as well as erosion, contributed to exhumation of the External Betics (e.g., Meijninger and Vissers, 2007).

The Prebetic area is characterized by the Cazorla-Alcaraz-Hellín structural arc (Fig. 1), which developed during the transition from Middle to Upper Miocene (Rodríguez-Pascua et al., 2000). It is constituted by NE-SW trending and SE dipping normal faults and NW-SE trending strike-slip dextral faults perpendicular to the fold axes. Among these sets, the tectonic system composed by the NE-SW trending Alto Guadalquivir fault and the NW-SE trending Socovos-Calasparra fault separates the Internal and External Prebetic Zones (Fig. 1).

2.2 The Betic Zn-Pb ore deposits

In the Betic Cordillera, the numerous Zn-Pb deposits and occurrences (Fig. 1) made this region of economic importance for the extraction of base metals. Mineralogically, these deposits can be grouped as sulfide and non-sulfide ores.

2.2.1 Sulfide Zn-Pb ore deposits

Three major types of Zn-Pb sulfide deposits are recognized in the Betic Cordillera (Fig. 1): i) Zn-(Fe-Pb) MVT deposits related to hydrothermal dolomites hosted in Lower Cretaceous carbonates of the Prebetic Zone (Navarro-Ciurana et al., 2015b; 2016); ii) stratabound (F)-Zn-Pb-Fe MVT deposits hosted in hydrothermally dolomitized Triassic limestones of the Alpujárride Complex (e.g., Fenoll, 1987); and iii) Zn-Pb-Fe-(Ag) epithermal deposits hosted in Triassic carbonates and related to Late-Tertiary subvolcanic rocks (e.g., Oen et al., 1975).

The most important stratabound (F)-Zn-Pb-Fe MVT deposits hosted in hydrothermally dolomitized Triassic limestones of the Alpujárride Complex are located at Sierra de Lújar, Sierra de Gádor and Sierra de Baza (Delgado et al., 1971; Espí, 1977; Ovejero et al., 1982; Tona, 1973; Torres-Ruiz et al., 1985). Other less economic deposits are present at Sierra de las Estancias, northwestern edge of Sierra Nevada, Sierra Tejada, Sierra Almijara, Cerro del Toro (Motril), Turón and Beninar area (Fig. 1) (Gervilla et al., 1985; Higueras et al., 1981; Martín and Torres-Ruiz, 1985, 1982; Morales-Ruano et al., 1996). The Sierra de Cartagena, Sierra de Mazarrón and Sierra de Almagrera are characterized by economically important epithermal deposits (Oen et al., 1975). Also, other Zn-Pb deposits formed by hydrothermal events are described in the Alpujárride Complex in the vicinity of the Vélez Rubio, in the areas of Sierra Alhamilla

and Sierra del Cantar, as well as in the Subbetic Complex in the vicinity of Zarzadilla de Totana town (Fig. 1).

2.2.2 Non-sulfide Zn-Pb ore deposits

The non-sulfide Zn-Pb ore systems appear related to or derived from primary sulfide ores. The most relevant non-sulfide Zn-Pb ores are associated with MVT deposits and occur in the Riópar area, at the Northern edge of the Sierra de Segura (Fig. 1). In the late XVIII century, the "Reales Fábricas de Alcaraz" brass factory was created, constituting the second one of this type in Europe. Ore production from these mines was very irregular over the years, for example: i.e. in 1850 the Zn production was of 1,100 t (Claramunt-González and Zúñiga-Rodríguez, 2011). Other calamine ores related to MVT mineral deposits, exploited in the mid of the XIX century, have been identified in the Sierra de Gádor, Sierra de Turón-Beninar, Cerro del Toro, Sierra de Almijar and Sierra de Baza within the Alpujarride Carbonate Complex (Fig. 1). Non-sulfide Zn occurrences associated with manto and epithermal mineral deposits have been described at La Union, in Sierra de Cartagena (Arribas and Tosdal, 1994; Manteca and Ovejero, 1992). Navan Mining Company reported a resource of 2.2 Mt at 3.5% Zn in the oxide zone of the epithermal Mazarrón deposit. Evidence of calamine mining was also found in Sierra Almagrera and Lorca (Fig. 1).

3 The Riópar MVT mineralization

The hypogene Zn-(Fe-Pb) sulfides in the Riópar area appear enclosed in stratabound and patchy hydrothermal dolostones, which cover an area of a 1.6 km^2 replacing a carbonate sequence of Upper Jurassic (Middle Kimmeridgian to Tithonian) to Lower

Cretaceous (Berriasian to Lower Aptian) age (Navarro-Ciurana et al., 2016) (Fig. 2). The main Zn-(Fe-Pb) mineralization is found in the Upper Member of the Puerto Lorente Formation (Upper Berriasian to Lower Valenginian) distributed in three mining complexes (Figs. 2 and 3): i) San Agustín, which consists of two ore bodies named "Sg1" and "Sg2"; ii) Rosita (Ro), which is located in the easternmost zone of the studied area. The ore body extension is unknown as outcrops are almost covered by vegetation and recent sediments; and iii) San Jorge, situated in the central part of the studied area, which contains different small ore bodies, which are grouped in three mines (Sj1, Sj2, Sj3). The real dimensions of the deposit are difficult to evaluate due to their irregular shape and vertical extension. However, an approximated mean dimension of 50 to 100 m in length, 20 to 30 m in width and 20 to 50 m in height is estimated considering the accessible mining works and comparing with historical mining reports (De Botella y Hornos, 1868; De la Escosura, 1845; Pellicio, 1845), has been deduced (Fig. 3).

The sulfide Zn-(Fe-Pb) deposits are distributed along the footwall block of the W-E-trending and S-dipping San Jorge extensional fault (SJF). The associated hydrothermal dolomitization (fluid inclusion T_h's around 205ºC: Navarro-Ciurana et al., 2016) is limited by the NW-trending Socovos fault (SF) (Figs. 2 and 3). The SJF seem to have focused the hydrothermal dolomitizing and ore-bearing fluids, indicating a structural control for fluid flow. The Upper Jurassic to Lower Cretaceous succession does not crop out in the hanging block of the San Jorge fault; it cannot be confirmed if this zone was affected by the same dolomitizing and mineralizing process (Navarro-Ciurana et al., 2016). The most important morphology of the sulfide ore bodies is represented by discordant lenses with NW-SE direction and dipping around 50º to the south, crosscutting the nearly horizontal stratification with a gentle S-dip (San Agustín

and San Jorge ores: Figs. 3a and 3c). Also, in some zones, small branching stratiform lenses occur as offshoots. Mineralization occurs as open space fillings in fractures forming cm- to mm-size veins and veinlets (Fig. 4a), as disseminated replacements of the hydrothermal host-dolomites (Figs. 4b and 4e), and cementing breccia zones (Fig. 4c). According to Navarro-Ciurana et al. (2016) the hypogene mineral paragenesis consists of: i) early dolomite**,** with transitions of planar-s (subhedral) replacive (ReD) and planar-e (euhedral) light sucrosic (SuD) dolomite-types (Figs. 4a and 4d); ii) early non-planar saddle dolomite (SaD-I) (Fig. 4d); iii) Zn-(Fe-Pb) ores composed of marcasite, sphalerite and minor galena (Figs. 4d and 4e); iv) late non-planar saddle dolomite (SaD-II) (Figs. 4c, 4d and 4e); v) late dolomite which consists of planar-e porphyrotopic (PoD) replacing sphalerite (Fig. 4f); and vi) planar-s cloudy cement (CeD).

4 Analytical methods

Hand samples were collected from underground workings, dumps and surface outcrops from all mineralized areas. The macroscopic identification of calamines was possible with Zinc Zap (3% potassium ferricyanide and 0.5% diethylaniline dissolved in 3% oxalic acid) which results in orange to red colorations of the rock when zinc carbonate and silicate minerals are present. Also, fluorescence light lamps were used in the lab for the characterization of some non-sulfide zinc minerals.

145 polished thin sections of both sulfide-rich and non-sulfide ores, as well as of host-rocks and dolomites related to Zn-(Fe-Pb) ores, were studied in detail using transmitted and reflected light petrographic microscopy at the *Departament de Geología* of the *Universitat Autònoma de Barcelona* (UAB). Selected thin sections were

previously half stained with alizarin red-S and potassium ferricyanide in order to distinguish calcite from dolomite and their ferroan equivalents. Cathodoluminescence (CL) analyses were performed in representative polished thin sections for Zn/Pb carbonate mineral characterization using a Technosyn 8200 MarkII cold-cathode electron-gun mounted on a polarizing microscope at the *Departament de Geoquímica, Petrologia i Prospecció Geològica* of the *Universitat de Barcelona* (UB). The electron beam was accelerated at 10-15 kV with a 400-500 mA beam current.

X-ray diffraction (XRD) analyses were carried out on 8 bulk powdered samples, for their mineralogical characterization, using an X'Pert-Philips diffractometer. The analyses were performed with a scanning velocity of 0.5º/min and CuKα monochromatic radiation at 40 kV and 30 mA at the *Servei de Difracció de Raig X* of the *UAB*. The software X'Pert was used to evaluate the analyzed spectra.

Representative polished thin sections were investigated in a Zeiss EVO MA 10 scanning electron microscopy (SEM) with accelerating voltage of 20kV at the *Servei de Microscòpia* at *UAB*. The identification and characterization of the different mineral phases were performed by qualitative analyses using energy-dispersive spectrometer (EDS) with a medium count time of 30s for analysis. A JEOL JXA 8900 electron microcroprobe at ITCS *Centro Nacional de Microscopía Electrónica*, Madrid, has been used for non-sulfide Zn-Pb and oxide mineral chemistry analysis. The instrument operated in WDS mode, at 20 kV accelerating voltage, 10nA beam current and with a beam diameter of less than 2µm. The counting time on peak and backgrounds were 15 and 5 seconds, respectively.

Smithsonite and calcite were separated by hand picking under a stereomicroscope and different dolomite types were sampled using a microdrilling device for carbon and oxygen isotope analysis, performed at the *Centres Científics i*

Tecnològics at UB (CCiTUB). For C and O isotope compositions, following the CO_2 extraction method of McCrea (1950), up to 30 mg of sample was reacted with anhydrous phosphoric acid (H_3PO_4) at 50ºC, and the collected CO_2 was analyzed in a Finnigan MAT Delta S thermal ionization mass spectrometer. The $\delta^{13}C$ values are reported as per mil (‰) relative to the Vienna-PeeDee Belemnite (V-PDB), whereas oxygen values are reported in δ ‰ relative to Vienna-Standard Mean Ocean Water (V-SMOW). The standard deviation was better than ±0.1‰ (1σ) for both $\delta^{13}C$ and $\delta^{18}O$.

Sulfur isotopic compositions were determined on hand picked sphalerite (*n*=10), galena (*n*=3), marcasite (*n*=4) and gypsum (*n*=1). Analyses were performed at the CCiTUB, using an on-line elemental analyzer (EA)-continuous flow-isotope ratio mass spectrometer (IRMS), with a precision better than ±0.1 per mil. The isotope ratios were calculated using the NBS127, IAEAS1, and IAEAS3 standards and reported relative to the Vienna-Canyon Diablo Troilite (V-CDT) standard.

5 Non-sulfide occurrences, mineralogy and textures

In the shallowest mining levels of the Riópar deposits, non-sulfide minerals are found as massive "red calamine" ore, principally as a mixture of smithsonite, iron oxi-hydroxides and cerussite. Non-sulfide minerals are found replacing partially or totally the Zn-(Fe-Pb) sulfides lenses (Fig. 5a) and filling fractures developing cockade calamine vein textures (Fig. 5b). Also, non-sulfide mineralization occurs as calamine microkarst- and porosity-infills (mainly smithsonite and hydrozincite) within the host-dolostone. Abundant Fe oxi-hydroxides mixed with minor smithsonite and cerussite characterize the upper parts of the sulfide ore bodies, suggesting a "gossan", with red-brown spongy textures. Locally gypsum is found here as accessory mineral (Fig. 5c). The non-sulfide ore bodies seem to be distributed according to three main structural

directions: i) N-S trending network fractures associated with major N-S faults (Fig. 3), ii) NW-SE fractures associated with replacement of discordant sulfide Zn-(Fe-Pb) ore-bearing lenses (Fig. 5c) and iii) stratiform horizons that correspond to replacements of concordant Zn-(Fe-Pb) sulfides (Fig. 5d). Furthermore, newly discovered gossan, never exploited nor described in the literature, has been found within the Arroyo de los Anchos Fm (Barremian to Lower Aptian) in the westernmost part of the studied area, near Fuente de la Calentura (FC; Fig. 2). The gossan is characterized by superficial crusts of Fe oxi-hydroxides.

The mineralogical phases of the non-sulfide Zn-(Fe-Pb) ores recognized in the Riópar mining area are smithsonite, hydrozincite, cerussite, goethite and hematite. Other accessory minerals associated with calamine ores are gypsum and calcite. The list of all minerals that have been detected at Riópar calamines is shown in Table 1. The data have been compiled from petrographic observations (optical and electronic microscopy) and X-ray diffraction analyses.

5.1 Smithsonite and hydrozincite

Smithsonite is the economically most abundant non-sulfide Zn-carbonate in the Riópar ore deposits (Table 1). Three smithsonite-types have been distinguished on the basis of color and textures.

Type I (Sm-I) is not very common and has been identified in samples of the “red calamine” ore type and in “gossan” mineralization. The reaction with Zinc Zap is strong, producing intense red-brownish to orange colors (Fig. 6a). It consists of anhedral microcrystalline brown aggregate crystals of less than 20 µm in length, developing crusts (Fig. 6b) partially or completely replacing colloform or granular aggregates of

sphalerite (Fig. 6c). It shows as a homogeneous bright to dull dark blue cathodoluminescence (Fig. 6d) and white to yellowish fluorescence.

Type II (Sm-II) has been observed in “red calamine” ore type and as a minor phase in “gossan” ore. It consists of botryoidal aggregates of brownish-red color crystals with a rugged appearance in hand sample (Fig. 6e). The reaction with Zinc Zap is strong, showing intense red colors. The botryoids (100 to 500 µm in size) are formed by gray polycrystalline subhedral microaggregates of smithsonite crystals (Fig. 6f), commonly with slightly rounded faces and locally with corroded crystal surfaces. Fe oxi-hydroxide globular concretion textures occur on these surfaces. This type of smithsonite replaces partially or totally colloform and crystalline sphalerite (Fig. 6f) and is fluid inclusion free. Sm-II form aggregates of microcrystals that are less than 10 µm long (Fig. 6g). In addition, CL observations revealed alternations of blue and pinkish luminescence domains (Fig. 6h) and is not fluorescent under UV light.

Type III (Sm-III) present as “rice-shaped grains” (Stara et al., 1996; Boni and Large, 2003), is very common. The reaction with Zinc Zap results in feeble reddish colors. It consists of botryoidal aggregates with colors ranging from white to grayish white often with a silky aspect (Fig. 7a). Most of the botryoids, which exhibit undulatory extinction, reach 1 mm in size (Fig. 7b) but, exceptionally, they may reach 1 cm in length; crystals observed under SEM (Fig. 7c) consist of rhombohedral microcrystals less than 40 µm (Fig. 7d). This smithsonite type has been detected infilling open cavities, porosity (Figs. 7b and 7d), fractures (Fig. 8a) and cementing dolomite breccias (Fig. 7e) as “gray calamine” ore. It shows markedly zoned, bright to dark blue luminescence with pink alternating bands (Fig. 7e) and white to yellowish fluorescence.

Hydrozincite is a rare mineral at Riópar (Table 1) and is found associated with smithsonite. On hand sample it appears as milky white botryoidal crusts showing intense red colorations with the Zinc-Zap reactive application. Under fluorescence microscopy it shows bright white to pale-blue colors. Hydrozincite occurs infilling open cavities and porosity, overgrowing the different smithsonite-types and saddle dolomite crystals (Fig. 7f).

5.2 Cerussite

The only Pb-carbonate phase identified at Riópar is cerussite (Table 1). Under the petrographic microscope it is recognized as colorless crystals associated with cubo-octahedral galena (Fig. 4e). Two cerussite-types have been distinguished on the basis of occurrence, cathodoluminescence colors and textures.

Type-I (Cer-I) occurs as very fine microcrystalline aggregates of crustiform aspect. The individual crystals have less than 1µm in size. Under CL microscopy this type of cerussite reveled dull bluish luminescence (Fig. 8a) and replaces galena crystals along their cleavage planes and faces (Fig. 8b). Type-II (Cer-II) is less abundant and consists of botryoidal aggregate crystals of 30 to 200 µm in size. It is found in open cavities and fractures (Fig. 8b) forming concretionary structures associated with galena crystals. Under CL examination Cer-II shows a zoned bright light blue luminescence (Fig. 8a).

5.3 Goethite and hematite

The most common “gossan” mineral is goethite (Table 1), which is even more abundant than non-sulfide Zn minerals. Three goethite-types have been distinguished in the Riópar ore samples.

Type-I (Ght-I) consists of microcrystalline aggregates with crystallites of sizes smaller than 1µm; they show pale gray color in reflected light microscopy. This goethite-type occurs replacing marcasite, either radiating cockscomb or massive aggregate marcasite crystals along their cleavage and microfractures. It is observed forming boxwork textures preserving the original iron-sulfide features (Fig. 8c). Type-II (Ght-II) is composed of multiple acicular crystals forming plumose fans reaching 50µm in length. It commonly appears as dark brown to gray acicular crystallites under reflected light, replacing goethite type-I and into a lesser extent marcasite crystals (Fig. 8d). Type-III (Ght-III) occurs as colloform, globular and mammillary masses with concentric and radial fibrous internal structure. The botryoids have sizes larger than 200µm, showing dark gray to brown alternating bands under reflected light microscopy. They replace the previous goethite types and marcasite obliterating their original textures (Fig. 8d).

Hematite is a minor component that accompanies goethite in the more evolved "gossan" areas. It shows reddish to brownish colors replacing marcasite crystals (Fig. 8e) and is intergrown with goethite. Hematite occurs as microcrystalline masses with crystal sizes of less than 10µm.

5.4 Gypsum and calcite

Gypsum is a minor mineral phase (Table 1). It is found as cm-size translucid aggregate crystals filling fractures and secondary porosity within the "gossan", "red calamine" ores (Fig. 8f) and the host-dolostone.

Different calcite types are present in the Riópar ore deposits. They are all non-ferroan, as indicated by the pink staining color with the application of alizarin red-s and potassium ferricyanide. Type-I calcite (BrC) is brown colored with poorly packed,

equigranular and anhedral fine grain crystals. This calcite type occurs as non-selectively to selectively replacing saddle dolomite crystals (Fig. 8g), which is interpreted as formed by calcitization or dedolomitization processes. A second type of calcite (WhC) consists of densely packed crystals from medium to very coarse sizes (around 100µm), euhedral to subhedral in shape and light white color. WhC occurs as blocky cement, without a preferred orientation, along veinlets and microfractures associated with brecciation (Fig. 8g). The third type of calcite (YeC) forms yellow cm- to dm-size druses in vuggs and fractures in dolomite bodies (Fig. 8h).

6 Geochemical data

Different non-sulfide mineralogical phases were analyzed for their elemental and C and O isotopic composition. Also, sphalerite, marcasite, galena and gypsum were analyzed for their S isotopic composition. Results are summarized in Tables 2 and 3.

6.1 Mineral chemistry of relevant non-sulfide minerals

Results of smithsonite, cerussite and goethite microprobe analyses are listed in Table 2. Due to the common intergrowths between mineral phases, it was not always possible to measure the composition of single minerals, as occurs in other non-sulfide Zn-Pb-Fe ore deposits (e.g.: Boni et al., 2009b). Therefore, some analyses possibly record a mixture of minerals.

Smithsonite: WDS microprobe analyses was conducted on different smithsonite types (Sm-I, Sm-II and Sm-III) revealing a relatively chemical homogeneity (Table 2). Zn contents for both smithsonite-types is in the range of 56.18 to 68.71 wt.% ZnO, with an average of 58.93 ± 2.41 wt.% (n=2) for Sm-I, 63.57 ± 1.15 wt.% (n=24) and 60.10 ±

1.46 wt.% (*n*=18) for Sm-III. The Zn composition is therefore much lower than the stoichiometric value of 64.9 wt.% ZnO. Fe content in smithsonite was generally low (< 4 wt.% FeO), although Sm-I and Sm-II show a slightly higher Fe composition (0.01 to 3.52 wt.%) than Sm-III (0.02 to 1.08 wt.%). This difference is probably due to the presence of mixed Fe oxi-hydroxides. Among other trace elements detected, Pb, Ca and Mg reach significant amounts with 0.04 to 1.44 wt.% for PbO, 0.33 to 1.62 wt.% for CaO and 0.20 to 1.57 wt.% for MgO.

Three microprobe profiles have been performed across Sm-III (Fig. 9), for geochemical characterization of zoning observed under CL microscopy (Fig. 7e). The samples from San Jorge mine (Jo-22 sample: two profiles) show a geochemical pattern that differs from that of San Agustín deposit (Ro-33 sample: one profiles): the ZnO content is higher in San Jorge (58.79 to 61.77 wt.%) than in San Agustín (56.74 to 60.54 wt.%). In contrast, the MgO and CaO content of San Jorge smithsonite is lower (between 0.21 and 0.57 wt.% for MgO and 0.39 and 1.03 wt.% for CaO) than the observed in San Agustín (between 0.72 and 1.08 wt.% for MgO and 0.33 and 1.62 wt.% for CaO). The Sm-III from San Agustín mine shows a correlation between ZnO and CaO content. Commonly, the ZnO low content of some Sm-III bands correspond to a slight increase of CaO (Fig. 9), which may be caused by substitution of Zn by Ca. This distribution pattern has not been observed in Sm-III from San Jorge mine (Fig. 9).

Cerussite: it shows Pb contents within the 82.07 to 82.87 wt.% PbO range, with an average of 82.47 ± 0.57 wt.%, close to its stoichiometric value of 83.53 wt.% PbO. Sr is also commonly present in the lattice of the Riópar cerussite (between 0.78 and 0.81 wt.%). It also contains CaO (0.06 and 0.29 wt.%) as well as minor to trace contents of Zn, Ba and Na (Table 2).

Goethite: iron concentration varies between 63.96 to 77.75 wt.% FeO, with averages that differ in the different goethite types: 71.05 ± 6.41 wt.% for Gt-I, 76.07 ± 2.60 wt.% for Gt-II and 74.16 ± 1.08 wt.% for Gt-III. These Fe oxi-hydroxides commonly contain high values of zinc, ranging from 0.73 to 6.02 wt.% ZnO, and in some cases, they also present high concentrations of lead with a maximum of 3.19 wt.% PbO. Traces of Ca, Sr, Mg and Ba have also been identified (Table 2).

6.2 Stable isotope systematics

The stable isotope (C, O) analyses of host-rocks, carbonate-Zn minerals and calcites were performed in order to characterize the fluid responsible for the non-sulfide mineralization. Also, S-isotope analyses were carried out to identify the origin of gypsum.

6.2.1 Carbon and oxygen isotopes

Limestone and marls (Middle Member of Sierra del Pozo and Cerro Lobo Formations), considered the host rocks of hydrothermal dolomites and hypogene sulfides, present $\delta^{13}C$ and $\delta^{18}O$ values between +0.5 and +3.2‰ and from +27.6 and +30.9‰, respectively (Table 3, Fig. 10). These values are in agreement with those reported by Veizer et al. (1999) for marine limestones of Upper Jurassic to Early Cretaceous age (Fig. 10). $\delta^{13}C$ and $\delta^{18}O$ values of hydrothermal dolomites (ReD-SuD, SaD) associated with Zn-(Fe-Pb) MVT ore range from -0.4 to +0.9‰ and from +25.1 to +27.6‰ respectively (Table 3, Fig. 10).

The $\delta^{13}C$ values of different smithsonite types exhibit a considerable range of -6.3 to +0.4‰ (Table 3, Figure 10). Moreover, the carbon isotopic composition varies with smithsonite types: i) Sm-I $\delta^{13}C$ exhibit values of -5.4 and +0.4‰ (n=2); ii) Sm-II

display values between -4.3 and -2.7‰; and iii) Sm-III is lighter with $\delta^{13}C$ values of -6.3 to -3.5‰ (*n*=4). In contrast, $\delta^{18}O$ values exhibit a small range, from +27.8 to +29.6‰, with an average of +28.8±0.6‰: Sm-I varies from +28.9 and +29.3‰; Sm-II has a $\delta^{18}O$ values between +27.8 and +29.0‰, whereas Sm-III displays a range of O isotopes from +28.5 and +29.6‰ (Table 3, Fig. 10). The calcite cements (YeC) show $\delta^{13}C$ values of -7.3 and -7.0‰ and $\delta^{18}O$ of +23.9 and +24.4‰ (Table 3, Fig. 10).

6.2.2 Sulfur isotopes

Sulfur isotope analyses have been carried out on sphalerite, galena and marcasite crystals as well as in gypsum. Analytical results are presented in Table 3 and shown in Figure 11. Marcasite $\delta^{34}S$ ranges from -7.5 to -5.8‰, and is isotopically lighter than sphalerite and galena, which $\delta^{34}S$ range from -2.2 to +3.5‰ and -2.8 and -2.4‰ respectively. $\delta^{34}S$ of gypsum has a value of +0.1‰, which is very similar to the sphalerite $\delta^{34}S$ average value.

7 Discussion

7.1 Non-sulfide paragenetic sequence

The mineral paragenetic sequence has been established on the basis of macroscopic observations and microscopic textural relationships among the different phases (Fig. 12). The non-sulfide Zn-(Fe-Pb) mineral assemblage (smithsonite, hydrozincite, goethite/hematite, cerussite and associated gypsum), occurrences (replacement of hypogene Zn-(Fe-Pb) sulfides, accumulations in microkarst cavities, secondary porosities and fractures as well as “gossan” ore formations) and C/O isotopic compositions of smithsonite (Fig. 10) suggest that calamines formed *in situ* as supergene mineralization. The paragenetic sequence of the hypogene sulfides related to

the hydrothermal dolomitization was previously stablished by Navarro-Ciurana et al. (2016).

The formation of supergene non-sulfide Zn-(Fe-Pb) corresponds to the development of the "gossan" and two types of calamine ores: "red and gray calamines" (Fig. 12). The occurrence of these two types of calamines is a common feature of many non-sulfide Zn deposits formed under supergene conditions, as occurs in the Moroccan High Atlas and the Southwest Sardinia calamine districts (e.g. Boni et al., 2003; Choulet et al., 2014). Furthermore, the formation of the Riópar "gossan" and "calamine" ores seem to be controlled by the abundance of hypogene sulfides. A later stage of dolomitization caused a decrease of abundance of sphalerite and consequently the Zn ions available for the non-sulfide Zn deposits formation. It is interesting to notice that anglesite and Zn-silicates (e.g., willemite, hemimorphite), which are a common phases of non-sulfide Zn-Pb ores (e.g., Boni et al., 2003; Choulet et al., 2004; Mondillo et al., 2014; Reichert, 2007), have not been detected in the Riópar "gossan" and "calamine" ore types.

The "gossan" ores are characterized by a mixture of abundant goethite and minor hematite, smithsonite, hydrozincite and cerussite. Commonly the microcrystalline goethite (Ght-I) precipitated replacing marcasite, before than acicular goethite plumose fans (Ght-II) and botryoidal goethite (Ght-III) (Fig. 8). Hematite is identified in the more highly evolved oxidized "gossan" parts suggesting that it probably formed subsequently than goethite.

The "red calamine" ore, which occurs as direct replacements of sulfides, is composed of abundant smithsonite (Sm-I and Sm-II), Fe oxi-hydroxides and minor microcrystalline cerussite (Cer-I). Smithsonite type-I always occurs previously than Sm-II, which conforms an evolution from anhedral to subhedral crystals (Fig. 6). Also,

microcrystalline goethite (Ght-I)/hematite occurs precipitating on Sm-II crystal faces and forming alternation bands (Fig. 6), suggesting that both phases are cogenetic (Fig. 12).

The relative temporal relationship between the "gossan" and "red calamine" formation is unclear. The "gossan" domain may correspond to a more evolved supergene phase than the "red calamine" zone, but both areas may have formed during the same stage (Fig. 12). This evolution may explain: i) the vertical distribution, characterized by "gossan" ores in the uppermost parts followed below by "red calamine" domains (Fig. 5a); ii) the observed transitions between "gossan" and "red calamines" (Fig. 5d); iii) the occurrence of the same secondary mineral association (Fe oxi-hydroxides-smithsonite-cerussite) in both domains; and iv) the dominance of primary sulfides and Zn- Pb-carbonates in "red calamine" ore. In any case, marcasite has been observed oxidized to goethite in many samples of hypogene ore in which sphalerite remains unaltered and without secondary minerals around the crystals. This feature suggests that marcasite is oxidized previously than sphalerite.

The "gray calamine" ore type, shows abundant mammelonary smithsonite (Sm-III) and, in a lesser extent botryoidal cerussite (Cer-II) and hydrozincite as precipitations in Sm-III crystal faces suggesting that formed after Sm-III. "Gray calamine" mineralization is observed precipitating in secondary porosity, filling fractures, cementing breccias and overgrowing dolomite, sphalerite, Sm-I, Sm-II and Cer-I crystal faces (Fig. 7). Therefore, this second stage of calaminization post-dates the "gossan" and "red calamine" formation (Fig. 12).

Gypsum aggregates have been recognized related with this third ore stage. On the other hand, the calcitization of saddle dolomite crystals (BrC: dedolomitization), and

precipitation of WhC and YeC druses are difficult to place in the paragenesis due the absence of textural relationships with the calaminization stage (Fig. 12).

7.2 Origin of fluids involved in the non-sulfide ore formation

Oxygen and carbon isotope data were used to estimate the origin of fluids and temperature associated to smithsonite and calcite precipitation. O isotope compositions of smithsonite at Riópar are similar to those from other known supergene non-sulfide Zn districts such as Iglesiente, SW Sardinia, Italy (Boni et al., 2003), Liège, Belgium (Coppola et al., 2008), Broken Hill, New South Wales, Australia (Böttcher et al., 1993; Gilg et al., 2008), Skorpion deposit, Namibia (Borg et al., 2003), Tui deposit, New Zealand (Robinson, 1974) and Vila Ruiva deposit, SE Portugal (Gilg et al., 2008) (Fig. 10). Nevertheless, C isotope compositions of the Riópar smithosnite are only similar to the smithsonite of Iglesiente, Liège, Skorpion and Tui districts (Fig. 10). This point to similar precipitation conditions of these deposits. Furthermore, the relatively uniform oxygen isotopic composition of the three types of smithsonite (Table 3, Fig. 10) may reflect the uniform source of O and constant temperature of the oxidizing fluid (Boni et al., 2003; Coppola et al., 2008; Gilg et al., 2008). In addition, the carbon isotopic signature from calcite and smithsonite are very similar but the oxygen isotopic signatures are clearly distinct, with $\delta^{18}O$ calcite values about 5‰ lower than smithsonite. The $\delta^{34}S$ composition of gypsum (0.1‰: Table 3), associated to the non-sulfide Zn-Pb minerals and Fe-(hydr)oxides, is similar to that of the primary sulfides (Table 3, Fig. 11). As expected, this is a clear indication of a sulfate source derived from the supergene oxidation of hypogene Zn-Fe-Pb sulfides.

7.2.1 Smithsonite and calcite precipitation temperature

Smithsonite in the Riópar district is considered of supergene origin (Fig. 10), which is consistent with description presented here. The exposition to meteoric waters may have started in late Miocene. Since then, the combined effect of regional uplift and erosion exhumed the External Betics (Braga et al., 2003; Meijninger and Vissers, 2007). The lower Cretaceous rocks and the MVT sulfides were then exposed and consequently more susceptible to the action of meteoric waters.

The weighted mean $\delta^{18}O$ isotopic composition values of actual meteoric waters in the Almeria and Murcia REVIP (*Red Española de Vigilancia de Isotópos en Precipitación*) stations of the Betic region are -4.67‰ and -4.94‰ respectively, which are consistent with the isotopic signature in the Mediterranean area (between -6.38 and -4.67‰) and with the high-resolution model maps of the present day annual mean $\delta^{18}O$ isotopic precipitation for Spain (Capilla et al., 2012; Díaz-Teijeiro et al., 2013; Rodríguez-Arévalo et al., 2011). Therefore, assuming that O isotopic composition of local meteoric waters (around -5.0‰) did not change significantly from Miocene to present day, a temperature of smithsonite precipitation can been calculated using the isotope fractionation equation between smithsonite and water of Gilg et al. (2008):

$$1000 \ln\alpha_{smithsonite\text{-}water} = 3.10(10^6/ T^2)-3.50$$

For a meteoric water $\delta^{18}O$ value of -5.0‰, calculated temperature range from 12 to 19ºC, which are in agreement with continental environment in a temperate climate (Boni et al., 2003; Coppola et al., 2009). A climate with alternating wet and dry cycles could promote the formation of weathering and oxidizing solutions (Hitzman et al., 2003), which would facilitate karstic development and replacement of the sulfides. Estimated temperatures are similar to those measured in other calamine deposits of southern Europe, as in Iglesiente (11 to 23ºC) and Vila Ruiva (12 to 16ºC) (Gilg et al., 2008).

Similarly, the calcite temperature of formation can be calculated using the oxygen isotope fractionation equation between calcite and water of O'Neil (1969):

$$1000 \ln\alpha_{calcite\text{-}water} = 2.78(10^6/ T^2)-2.89$$

Assuming the same O isotopic composition of local meteoric waters of -5.0‰, and using the obtained $\delta^{18}O$ values (+23.9 to +24.3‰: Table 3, Fig. 10), calculated temperatures range from 21.0 to 22.5ºC. Although these temperatures are slightly higher than those obtained for smithsonite precipitation, the calculated values for both minerals are only estimates and these differences may not necessarily represent different temperature conditions during precipitation. The coexistence (coprecipitation) of both minerals and their O-isotope composition are compatible with a precipitation from meteoric fluids during temperate climate conditions.

7.2.2 Source of carbon

The variation in $\delta^{13}C$ observed in smithsonite (from -6.3 to +0.4‰) can be interpreted as a result of carbon mixing between a ^{13}C-enriched and ^{13}C–depleted source, with a predominance of ^{13}C-depleted source of carbon. In contrast, the homogeneity of $\delta^{13}C$ composition of calcites (-7.3 to -7.0‰: Table 3, Fig. 10) suggests a dominant ^{13}C-depleted source.

The most abundant carbon source for ^{13}C-enriched values for Zn-supergene carbonates at Riópar are the host-limestones and the ReD-SuD and SaD dolomites as their $\delta^{13}C$ average values are +2.3±1.0‰, -0.2±0.6‰ and +0.1±0.3‰ respectively (Table 3, Fig. 10). The release of CO_2 by the dissolution of host-carbonates could have been promoted by acidic solutions generated during oxidation of sulfides (e.g., Williams, 1990). The carbon source of ^{13}C-depleted component in smithsonites and calcites (minimum $\delta^{13}C$ isotopic value around -7.0‰) is most probably organic matter

derived from decomposition of C_3 ($\delta^{13}C$ between -32.0 to -25.0‰: Deines, 1980) and/or C_4 ($\delta^{13}C$ between -14.0 to -10.0‰: Cerling and Quade, 1993) vegetation in soils covering the ore. Mixing between these two sources (organic and carbonates) may explain the carbon isotopic values of smithsonite and calcite. Also, a minor contribution of ^{13}C-depleted component from the oxidation of bacteria known to be active during supergene sulfide oxidation (e.g., Melchiorre and Enders, 2003) can not be ruled out.

7.3 Evolution of fluids and non-sulfide precipitation model

Meteoric water percolation was facilitated by the exhumation of the External Betics, from late Miocene to present, along three faults systems (Fig. 2): the NE-SW trending San Jorge fault, the NW-SE trending strike-slip Socovos fault which is still active, and minor N-S system faults, probably generated by the effect of the Alpine orogeny. In addition irregular porosity, frequently interconnected and related to the dolomitization processes, conferred a certain permeability to the host-dolostone away from the faults. All this, together with the discordant lens morphology of the primary sulfide ore contribute to the deep infiltration and circulation of meteoric waters, oxidation of sulfide and circulation of the resulting oxidized metal-bearing fluids that lead to the precipitation of non-sulfide ores. From the mineral paragenesis two supergene stages can be distinguished (Fig. 12): i) “red calamine” and “gossan” ore stage; and ii) “gray calamine” ore stage. A calcite and gypsum precipitations stage was also considered (Figs. 12 and 13). Although field and petrographic observations indicate that the Riópar “gray calamines” formed consecutively to the formation of “gossan” and “red calamines” (Fig. 12), multiple oxidation processes occurring simultaneously during the formation of these different ore types are not discarded, as suggested by Reichert and Borg (2008).

7.3.1 "Red calamine" and "gossan" ore formation

The first stage of supergene oxidation (Fig. 13) was constituted by a "red calamine" and "gossan" domains, which probably formed at different oxidizing degrees. These domains must have developed when meteoric fluids ($\delta^{18}O$ ~ -5‰) with dissolved O_2 infiltrated along faults and fractures as well as porosity (Fig. 13, 1), reaching and reacting with marcasite producing Fe^{2+}, Fe^{3+}, SO_4^{2-} and H^+ (Dold, 2003; Salmon, 2003) (Fig. 13, 2). Iron ions were trapped as iron oxi-hydroxides replacing marcasite crystals (Fig. 13, 3). Goethite precipitated under early acidic conditions, whereas hematite crystallized later on under neutral/buffered pH conditions (e.g., Choulet et al., 2014). This process leads to a pH decrease of the fluids, which were then buffered by the host-carbonates with heavy $\delta^{13}C$ signature. Carbonate dissolution and neutralization released Ca^{2+}, Mg^{2+} and bicarbonate into the solution preserving their ^{13}C-rich isotopic signature (Fig. 13, 4). Reaction involving organic matter from degradation of vegetation also occurred, generating $CO_{2(g)}$ and providing the fluid with a ^{13}C-poor isotopic signature (Fig. 13, 5), which is mixed with ^{13}C-rich isotopic signature fluids (Fig. 13, 6).

The oxidation of sphalerite and galena produced again some amounts of acidity (Fig. 13, 7), probably less than the oxidation of marcasite, which must have generated the largest sulfuric acid volumes (Bertorino et al., 1995; Dold, 2003; Salmon, 2003). Galena and sphalerite reacted not only with oxygen but preferentially with the oxidation products of the marcasite dissolution like $Fe_2(SO_4)_3$ (Fig. 13, 8). Consequently, Pb^{2+} and Zn^{2+} ions were released (Fig. 13, 7-8) and combined with carbonate ions (Fig. 13, 9). Under acid pH and high $P(CO_2)_g$ conditions, smithsonite and cerussite can precipitate (Choulet et al., 2014) (Fig. 13, 9). The Fe in the smithsonite that replaced sphalerite provided the iron to form the goethite concretions on smithsonite (Sm-I and mainly in

Sm-II) crystals (Fig. 13, 9). Smithsonite incorporated Pb, Ca and Mg as product of the simultaneous oxidation of galena and the dissolution of carbonates (Table 2). Also, the Pb^{2+} ions released by the oxidation of galena (Bertorino et al., 1995) combined with carbonate ions precipitating as cerussite (Fig. 13, 8). Because of their lower mobility, Pb ions were transported over short distances (Choulet et al., 2014) and, thus, cerussite (Cer-I) only occurs as galena replacements. The absence of anglesite in the Riópar supergene deposit may be explained by the dissolution of anglesite and/or a total replacement of anglesite by cerussite. After the oxidation of the sulfide ore and the precipitation of sulphates, the concentration of SO_4^{2-} decreased and the pH must have moved to basic conditions (Reichert, 2007). Therefore, cerussite became more stable then anglesite producing a replacement of Pb-sulfate by Pb-carbonate (Fig. 13, 9). As galena is a minor phase in the Riópar area the amounts of anglesite and cerussite generated in the initial stages of oxidation must have been small. Moreover, during the sulfide oxidation stage in Riópar, the availability of silica in the system was insufficient to form Zn-silicates.

When FeS_2 was partially or completely oxidized in the most surficial areas, and therefore generating the "gossan" domain, the partial dissolution of sphalerite and galena leads to a mobilization of metals towards domains of less advanced oxidation (e.g., "red and gray calamine" domains). This evolution, which is controlled by the water table depth and the infiltration of meteoric waters, may be progressive. Therefore, the "red calamine" domain may evolve into a "gossan" when the dissolution of sphalerite and the amount of Zn^{2+} ions released was high.

7.3.2 "Gray calamine" ore formation

The second stage of the supergene evolution is dominated by "gray calamine" ore formations (Fig. 13). The Zn^{2+} ions released by oxidation of sphalerite generated SO_4^{2-} ions (Fig. 13, 7-8), occurring after the partial or total oxidation of FeS_2 (Reichert and Borg, 2008). Because of the higher mobility of Zn ions, they can be transported over a long distance under acid pH and high $P(CO_2)_g$ conditions (Choulet et al., 2014) so that smithsonite (Sm-III) precipitated in any porosity of the ore bodies and/or further away into the host carbonate (Fig. 13, 10). Pb ions also migrated over short distances precipitating within the rocks porosities as botryoidal cerussite (Cer-II) (Fig. 13, 10). Smithsonite was replaced by hydrozincite in some instances by hydration process (Fig. 15, 11), when the partial pressure of $CO_{2(g)}$ was low enough (Takahashi, 1960).

7.3.3 Calcite and gypsum formation

Calcites precipitated by the action of abundant ^{13}C-poor fluids in places where this was the dominant source (Fig. 13, 12). The combination of Ca^{2+} from dissolved carbonates (Fig. 13, 4) and SO_4^{2-} from oxidized marcasite (Fig. 13, 2), sphalerite and galena (Fig. 13, 7-8), caused the precipitation of gypsum (Fig. 13, 13). According to Reichert and Borg (2008), the development of gypsum crystals, which may grow onto the host carbonates, leads to an armoring effect reducing the reactivity of host carbonates and stabilizing low pH-values within the oxidation zone.

8 Conclusions

The present work constitutes the first detailed study of a calamine deposit in the Betic Cordillera (SE Spain). It is focused on the mineralogical and geochemical characteristics of the Riópar non-sulfide mineralization in order to constrain the origin and evolution of the ore-forming fluids.

The Riópar Zn-(Fe-Pb) non-sulfide mineral assemblage consists of abundant smithsonite and Fe-(hydr)oxides, scarce cerussite, and minor hydrozincite. Textural relationships allowed to distinguish two supergene stages under oxidation conditions: i) "gossan" ore formation characterized by abundant Fe-(hydr)oxides and "red ore" with abundant smithsonite replacing sphalerite (Sm-I and Sm-II), associated Fe-(hydr)oxides and cerussite replacing galena (Cer-I); and ii) "gray ore" composed by botryoidal smithsonite (Sm-III), in some areas replaced by hydrozincite, and mammillary cerussite (Cer-II). Moreover, gypsum is found as encrustation precipitates in all three supergene ore stages.

The different smithsonite types have a uniform oxygen isotope composition (+27.8 to +29.6‰), pointing to a constant isotopic source and precipitation temperatures. Assuming a constant $\delta^{18}O$ value for meteoric waters of -5‰ (the present day value), calculated temperature of smithsonite precipitation ranges from 12 to 19ºC, somewhat lower than temperatures calculated for calcite formation (21 to 23ºC) and consistent with a temperate climate. In contrast, $\delta^{13}C$ values of smithsonite (-6.26 to +0.43‰) indicate precipitation by mixing of at least two carbon sources: CO_2 from the dissolution of host-dolostones and -limestones (^{13}C-enriched source) and CO_2 derived from decomposition of vegetation (^{13}C-depleted source). The carbon isotope signature of calcite is similar to the ^{13}C-depleted values obtained in smithsonite, suggesting a dominantly ^{12}C enriched source related to organic matter decomposition. The similarity of C and O isotope data between calamines from the temperate Southern Europe suggests that there was a common major event of sulfide oxidation.

A number of calamine occurrences are found in the Betics. Although there are no detailed mineralogical studies, geological environment and mineral precursors are similar to Riópar. On the other hand as uplift of the Betic Cordillera took place from

Late Miocene times it is possible that the formation of calamine deposits is contemporaneous in all this area. More detailed geological, mineralogical and isotopic studies of the Betic supergene non-sulfide Zn ore deposits would help to better understand the relationships between the regional tectonic uplift, erosion, water table levels and the supergene evolution of hypogene Zn sulfide ore deposits.

Acknowledgments

This research has been supported by the Spanish *Ministerio de Economía y Competitividad*, through the CGL2011-26488 project, and formed in the Geology PhD Program at *Universitat Autònoma de Barcelona* (MEE2011-0492). The authors would like to acknowledge Federico Ballesta (*Ciencia y Aventura*) for their support in the fieldwork. Dr. Juan Diego Martín is especially thanked for his help with CL observations. We also express our gratitude to Franco Pirajno and two anonymous reviewers for comments that significantly improve the quality of the manuscript.

References

Arribas, A.J., Tosdal, R.M., 1994. Isotopic composition of Pb in ore deposits of the Betic Cordillera, Spain: Origin and relationship to other European deposits. Econ. Geol. 89, 1074–1903. doi:10.2133/gsecongeo.89.5.1074

Balassone, G., Rossi, M., Boni, M., Stanley, G., McDermott, P., 2008. Mineralogical and geochemical characterization of nonsulfide Zn-Pb mineralization at Silvermines and Galmoy (Irish Midlands). Ore Geol. Rev. 33, 168–186. doi:10.1016/j.oregeorev.2006.06.001

Banks, C.J., Warburton, J., 1991. Mid-crustal detachment in the Betic system of southeast Spain. Tectonophysics 191, 275–289. doi:10.1016/0040-1951(91)90062-W

Barbero, L., López-Garrido, A.C., 2006. Mesozoic thermal history of the Prebetic continental margin (southern Spain): Constraints from apatite fission-track analysis. Tectonophysics 422, 115–128. doi:10.1016/j.tecto.2006.05.011

Bertorino, G., Caredda, A.M., Ibba, A., Zuddas, P., 1995. Weathering of Pb-Zn mine tailings in pH buffered environment. Water-rock Interact. Proc. Symp. Vladivostok, 859–862.

Boland, M.B., Kelly, J.G., Schaffalitsky, C., 2003. The Shaimerden supergene zinc deposit, Kazakhstan: A preliminary examination. Econ. Geol. 98, 787–795. doi: 10.2113/gsecongeo.98.4.787

Boni, M., Large, D., 2003. Nonsulfide zinc mineralization in Europe: An overview. Econ. Geol. 98, 715–729. doi:10.2113/gsecongeo.98.4.715

Boni, M., Gilg, H.A., Aversa, G., Balassone, G., 2003. The “Calamine” of southwest Sardinia: Geology, mineralogy, and stable isotope geochemistry of supergene Zn mineralization. Econ. Geol. 98, 731–748. doi:10.2113/gsecongeo.98.4.731

Boni, M., Gilg, H.A., Balassone, G., Schneider, J., Allen, C.R., Moore, F., 2007. Hypogene Zn carbonate ores in the Angouran deposit, NW Iran. Miner. Depos. 42, 799-820. doi: 10.1007/s00126-007-0144-4

Boni, M., Balassone, G., Arseneau, V., Schmidt, P., 2009a. The nonsulfide zinc deposit at Accha (Southern Peru): Geological and mineralogical characterization. Econ. Geol. 104, 267–289. doi:10.2113/gsecongeo.104.2.267

Boni, M., Schmidt, P.R., De Wet, J.R., Singleton, J.D., Balassone, G., Mondillo, N., 2009b. International Journal of Mineral Processing Mineralogical signature of

nonsulfide zinc ores at Accha (Peru): A key for recovery. Int. J. Miner. Process. 93, 267–277. doi:10.1016/j.minpro.2009.10.003

Boni, M., Mondillo, N., 2015. The “Calamine” and the “Others”: The great family of supergene nonsulfide zinc ores. Ore Geol. Rev. 67, 208–233. doi:http://dx.doi.org/10.1016/j.oregeorev.2014.10.025

Borg, G., Kärner, K., Buxton, M., Armstrong, R., van der Merwe, S.W., 2003. Geology of the Skorpion supergene zinc deposit, Southern Namibia. Econ. Geol. 98, 749–771. doi:10.2113/gsecongeo.98.4.749

Böttcher, M.E., Gehlken, P.L., Birch, W.D., Usdowski, E., Hoefs, J., 1993. he rhodochrosite–smithsonite solid-solution series from Broken Hill (NSW), Australia: geochemical and infrared spectroscopic investigations. Neues Jahrb. für Mineral. Monatshefte, 352–362.

Braga, J., Martín, J.M., Quesada, C., 2003. Patterns and average rates of late Neogene–Recent uplift of the Betic Cordillera. Geomorphology 50, 3–26. doi: 10.1016/S0169-555X(02)00205-2

Calvo, J.P., Elízaga, E., López-Martínez, N., Robles, F., Usera, J., 1978. El Mioceno superior continental del Prebético Externo: Evolución del Estrecho Norbético. Boletín Geológico y Min. 89, 407–426.

Capilla, J.E., Rodríguez-Arévalo, J., Castaño, S., Díaz-Teijeiro, M.F., Sánchez-Moral, R., Heredia, J., 2012. Mapping Oxygen-18 in Meteoric Precipitation over Peninsular Spain using Geostatistical Tools, in: 9th Conference on Geostatistics for Environmental Applications - geoENV2012. Valencia, Spain, pp. 1–7.

Cerling, T.E., Quade, J., 1993. Stable carbon and oxygen isotopes in soil carbonates, in: Swart, P.K., Lohmann, K.C., Mckenzie, J., Savin, S (Eds.), Climate change in

continental isotopic records. Amer. Geophys. Union Monogr. 78, pp. 217–231. doi:10.1029/GM078p0217.

Choulet, F., Charles, N., Barbanson, L., Branquet, Y., Sizaret, S., Ennaciri, A., Badra, L., Chen, Y., 2014. Non-sulfide zinc deposits of the moroccan high atlas: Multi-scale characterization and origin. Ore Geol. Rev. 56, 115–140. doi:10.1016/j.oregeorev.2013.08.015

Claramunt-González, J., Zúñiga-Rodríguez, A.I., 2011. Las minas de San Jorge y las Reales Fábricas de Alcaraz. Foresta 47-48, pp. 50–54.

Cole, P.M., Sole, K.C., 2002: Solvent extraction in the primary and secondary processing of zinc. J. South Afr. Inst. Min. Metall. 102, 451-456.

Coppola, V., Boni, M., Gilg, A.H., Strzelska-Smakowska, B., 2009. Nonsulfide zinc deposits in the Silesia-Cracow district, Southern Poland. Miner. Depos. 44, 559–580. doi:10.1007/s00126-008-0220-4

Coppola, V., Boni, M., Gilg, H.A., Balassone, G., Dejonghe, L., 2008. The “calamine” nonsulfide Zn-Pb deposits of Belgium: Petrographical, mineralogical and geochemical characterization. Ore Geol. Rev. 33, 187–210. doi:10.1016/j.oregeorev.2006.03.005

Daliran, F., Pride, K., Walther, J., Berner, Z.A., Bakker, R.J., 2013. The Angouran Zn (Pb) deposit, NW Iran: Evidence for a two stage, hypogene zinc sulfide-zinc carbonate mineralization. Ore Geol. Rev. 53, 373–402. doi:10.1016/j.oregeorev.2013.02.002

De Botella y Hornos, 1868. Descripción geológica-minera de las provincias de Murcia y Albacete.

Deines, P., 1980. The isotopic composition of reduced organic carbon, in: Fritz, P., Fontes, J.C. (Eds.), Handbook of environmental geochemistry, v. 1, Amsterdam, Elsevier, p. 329–406.

De la Escosura, L., 1845. De la mina de Zinc y fábricas de latón de S. Juan de Alcaráz junto a Riópar. Anales de Minas 3, 198-155.

Delgado, F., Ovejero, G., Jacquin, J.P., 1971. Localización estratigráfica y medio paleogeográfico de las mineralizaciones (galena y fluorita) de Sierra de Baza (Granada, Espana). I. Congr. Hisp. Luso Am. Geol. Ec. E-4–13, pp. 119–125.

Díaz-Teijeiro, M.F., Pérez-Zabaleta, E., Prado-Pérez, A., Bardasano-Picazo, L., Muñoz-Delavarga, D., Rodríguez-Arévalo, J., 2013. La Red Española de Vigilancia de Isótopos en la Precipitación (REVIP), in: XI Congreso Nacional Y IX Congreso Ibérico de Geoquímica. Soria, Spain, pp. 90–91.

Dold, B., 2003. Enrichment processes in oxidizing sulfide mine tailings: Lessons for supergene ore formation. Soc. Geol. Appl. to Miner. Depos. News 16, 10–15. doi:10.1016/S0375-6742(03)00182-1

Espí, J.A., 1977. Aspecto metalogenético de los criaderos de flúor-plomo de la Sierra de Gádor (Almeria). Esc. Tec. Sup. Ing. Min., Madrid.

Fallot, P., 1948. Les Cordillères Bétiques. Estud. Geol. 6, 259–279.

Fenoll Hach-Alí, P., 1987. Los yacimientos de F-Pb-Zn-Ba del sector central de la Cordillera Bética. Universidad de Granada.

García-Hernández, M., Lopez-Garrido, a. C., Rivas, P., Sanz de Galdeano, C., Vera, J. a., 1980. Mesozoic palaeogeographic evolution of the external zones of the Betic Cordillera. Geol. en Mijnb. 59, 155–168.

Gervilla, F., Torres-Ruiz, J., Martín, J.M., Fenoll Hach-Ali, P., 1985. Los depósitos de F-(Pb-Zn) del Coto Minero de Turón (Granada). Bol. Soc. Esp. Miner. 8, 219–228.

Gilg, H.A., Boni, M., Hochleitner, R., Struck, U., 2008. Stable isotope geochemistry of carbonate minerals in supergene oxidation zones of Zn-Pb deposits. Ore Geol. Rev. 33, 117–133. doi:10.1016/j.oregeorev.2007.02.005

Gnoinski, J., 2007. Skorpion zinc: optimization and innovation. J. South Afr. Inst. Min. Metall, 107, 657-662.

Grandia, F., Canals, À., Cardellach, E., Banks, D.A., Perona, J., 2003a. Origin of ore-forming brines in sediment-hosted Zn-Pb deposits of the Basque-Cantabrian basin, Northern Spain. Econ. Geol. 98, 1397–1411. doi:10.2113/gsecongeo.98.7.1397

Grandia, F., Cardellach, E., Canals, À., Banks, D.A., 2003b. Geochemistry of the fluids related to epigenetic carbonate-hosted Zn-Pb deposits in the Maestrat basin, Eastern Spain: Fluid inclusion and isotope (Cl, C, O, S, Sr) evidence. Econ. Geol. 98, 933–954. doi:10.2113/gsecongeo.98.5.933

Groves, I.M., Carman, C.E., Dunlap, W.J., 2003. Geology of the Beltana willemite deposit, Flinders Ranges, South Australia. Econ. Geol. 98, 797–818. doi:10.2113/gsecongeo.98.4.797

Heyl, A.V., Boizon, C.N., 1962. Oxidized zinc deposits of the United States, part 1.General geology. U.S. Geol. Surv. Bull. 1135-A, 52 pp.

Higueras, P., Fenoll Hach-Ali, P., Rodriguez-Gordillo, J., 1981. Geologia, mineralogia y genesis del yacimiento de Pb-Zn del Cerro del Toro (Motril, Granada). Tec. Madrid 44, 65–76.

Hitzman, M.W., Reynolds, N.A., Sangster, D.F., Allen, C.R., Carman, C.E., 2003. Classification, genesis, and exploration guides for nonsulfide zinc deposits. Econ. Geol. 98, 685–714. doi:10.2113/gsecongeo.98.4.685

Hosseini, S.H., 2008. Physicochemical Studies of Oxide Zinc Mineral Flotation. (dissertation) University of Technology, Lulea.

Large, D., 2001. The geology of nonsulphide zinc deposits - an overview. Erzmetall 54, 264–276.

Manteca, J.I., Ovejero, G., 1992. Los yacimientos Zn, Pb, Ag, Fe, del distrito minero de la Unión-Cartagena, Bética Oriental, in: García-Guinea, J., Martínez-Frías, J. (Eds.), Recursos Minerales de España. CSIC, Madrid, pp. 1085–1102.

Martín, J.M., Torres-Ruiz, J., 1985. Stratigraphic, sedimentological and petrological controls on the stratiform and/or stratabound F-Pb-Zn-Ba deposits of the Triassic of the Alpujgtrrides (Betic Cordillera, Southern Spain), in: 6th Europ. Regional Meet. IAS, Lleida (Spain), Abstracts, pp. 277–280.

Martín, J.M., Torres-Ruiz, J., 1982. Algunas consideraciones sobre la convergencia de medios de depósito de las mineralizaciones de hierro y plomo-zinc-fluorita de origen sedimentario encajadas en rocas triasicas de los Complejos Nevado-Filábride y Alpujárride del sector central de la Cordillera Bética. Bol. Geol. Min. Madrid 93, 314–329.

Martín, J.M., Torres-Ruiz, J., Fontboté, L., 1987. Facies control of strata-bound ore deposits in carbonate rocks: The F-(Pb-Zn) deposits in the Alpine Triassic of the Alpuj rrides, southern Spain. Miner. Depos. 22, 216–226. doi: 10.1007/BF00206613

Meijninger, B.L.M., Vissers, R.L.M., 2007. Thrust-related extension in the Prebetic (Southern Spain) and closure of the North Betic Strait. Rev. la Soc. Geológica España 20, 119–136.

Melchiorre, E.B., Enders, M.S., 2003. Stable isotope geochemistry of copper carbonates at the Northwest Extension deposit, Morenci District, Arizona: Implications for conditions of supergene oxidation and related mineralization. Econ. Geol. 98, 607–621. doi:10.2113/gsecongeo.98.3.607

Mondillo, N., Boni, M., Balassone, G., Joachimski, M., Mormone, A., 2014. The Jabali nonsulfide Zn-Pb-Ag deposit, western Yemen. Ore Geol. Rev. 61, 248–267. doi:10.1016/j.oregeorev.2014.02.003

Monteiro, L.V.S., Bettencourt, J.S., Juliani, C., de Oliveira, T.F., 2007. Nonsulfide and sulfide-rich zinc mineralizations in the Vazante, Ambrósia and Fagundes deposits, Minas Gerais, Brazil: Mass balance and stable isotope characteristics of the hydrothermal alterations. Gondwana Res. 11, 362–381. doi:10.1016/j.gr.2006.04.017

Montenat, C., Ott d'Estavou, P., Pierson D'Autrey, P., 1996. Miocene basins of the eastern Prebetic zone: some tectonosedimentary aspects, in: Friend, P.F., Dabrio, C.J. (Eds.), Tertiary Basins of Spain: The Stratigraphic Record of Crustal Kinematics. Cambridge University Press, pp. 346–352.

Morales Ruano, S., Both, R., Fenoll Hach-Ali, P., 1995. Fluid evolution and mineral deposition in the Aguilas-Sierra Almagrera base metal ores, southeastern Spain, in: Pasava, J., Kribek, B., Zak, K. (Eds.), Mineral Deposits: From Their Origin to Their Environmental Impacts. Balkema, Rotterdam, The Netherlands, pp. 365–368.

Morales-Ruano, S., Touray, J.C., Barbanson, L., Fenoll Hach-Ali, P., 1996. Génesis de las mineralizaciones de Ge asociadas a esfalerita portadoras de fluidos "incompatibles" del Cerro del Toro (Alpujárride, SE de España). Geogaceta 20(7), 1567–1570.

Navarro-Ciurana, D., Corbella, M., Gómez-Gras, D., Griera, A., Vindel, E., Cardellach, E., 2015a. Relationship between Dolomite Textures and Formation Temperature - Insights from the Riópar Area (Betic basin, SE Spain). Ext. absract Tu N110 07, Present. 77th Eur. Assoc. Geosci. Eng. Conf. Exhib. 2015. doi:10.3997/2214-4609.201412661

Navarro-Ciurana, D., Corbella, M., Griera, A., Gómez-Gras, D., Vindel, E., Daniele, L., Cardellach, E., 2015b. Geochemical evidences and heat-transport simulations for warm fluid involvement in the formation of Riópar MVT deposit (Prebetic Basin , SE Spain). Extended absract S3-P18, presented at the Society for Geology Applied to Mineral Deposits 13th Biennial Meeting, Nancy, France.

Navarro-Ciurana, D., Corbella, M., Cardellach, E., Vindel, E., Gómez-Gras, D., Griera, A., 2016. Petrography and geochemistry of fault-controlled hydrothermal dolomites in the Riópar area (Prebetic Zone, SE Spain). Mar. Pet. Geol. 71, 310–328. doi:10.1016/j.marpetgeo.2016.01.005

O'Neil, J.R., 1969. Oxygen Isotope Fractionation in Divalent Metal Carbonates. J. Chem. Phys. 51, 5547–5558. doi:10.1063/1.1671982

Oen, I.S., Fernández, J.C., Manteca, J., 1975. The Lead-Zinc and associated ores of La Unión, Sierra de Cartagena, Spain. Econ. Geol. 70, 1259–1278. doi:10.2113/gsecongeo.70.7.125

Ovejero, G., Tona, F., Martín, J.M., Gutierrez, A., Jacquin, J.P., Servejean, G., Zubiaur, J.F., 1982. Las mineralizaciones estratiformes F_2Ca-Pb en las dolomias triásicas de Sierra de Lújar, Granada (Cordilleras Beticas, España). Bol. Geol. Min. Madrid 93, 475–495.

Pedrera, A., Marín-Lechado, C., Galindo-Zaldívar, J., García-Lobón, J.L., 2014. Control of preexisting faults and near-surface diapirs on geometry and kinematics of fold-and-thrust belts (Internal Prebetic, Eastern Betic Cordillera). J. Geodyn. 77, 135–148. doi:10.1016/j.jog.2013.09.007

Pellicio, R.P., 1845. Minas de Zinc de San Juan de Alcaraz en la provincia de Albacete. Boletín oficial de minas 19, 323–326.

Reichert, J., Borg, G., 2008. Numerical simulation and a geochemical model of supergene carbonate-hosted non-sulphide zinc deposits. Ore Geol. Rev. 33, 134–151. doi:10.1016/j.oregeorev.2007.02.006

Robinson, B.W., 1974. The origin of mineralization at the Tui mine, Te Aroha, New Zealand, in the light of stable isotope studies. Econ. Geol. 69, 910–925. doi: 10.2113/gsecongeo.69.6.910

Rodríguez-Arévalo, J., Díaz-Teijeiro, M.F., Castaño, S., 2011. Modelling and mapping oxigen-18 isotope composition of precipitation in Spain for hydrologic and climatic applications, in: International Symposium on Isotopes in Hydrology, Marine Ecosystems and Climate Change Studies. Monaco, pp. 171–177.

Rodríguez-Pascua, M.A., Calvo, J.P., De Vicente, G., Gómez-Gras, D., 2000. Soft-sediment deformation structures interpreted as seismites in lacustrine sediments of the Prebetic Zone, SE Spain, and their potential use as indicators of earthquake magnitudes during the Late Miocene. Sediment. Geol. 135, 117–135. doi:10.1016/S0037-0738(00)00067-1

Salmon, S.U., 2003. Geochemical modelling of acid mine drainage in mill tailings: Quantification of kinetic processes from laboratory to field scale. Ph.D. KTH Land and Water Resource Engeneering, pp. 51.

Sánchez-Valcerde, J., Fernández-Leyva, C., Navarro, R., 2013. Síntesis de los principales recursos minerales metálicos de la Cordillera Bética en Andalucía y las zonas de potencialidad minera. Geogaceta, 54, 79-82.

Santoro, L., Boni, M., Herrington, R., Clegg, A., 2013. The Hakkari nonsulfide Zn-Pb deposit in the context of other nonsulfide Zn-Pb deposits in the Tethyan Metallogenic Belt of Turkey. Ore Geol. Rev. 53, 244–260. doi:10.1016/j.oregeorev.2013.01.011

Stara, P., Rizzo, R., Tanca, G.A., 1996. Iglesiente-Arburese, miniere e minerali, Ente Minerario Sardo, v.I, pp. 238.

Takahashi, T., 1960. Supergene alteration of zinc and lead deposits in limestone. Econ. Geol. 55, 1084–115. doi:10.2113/gsecongeo.55.6.1083

Tona, F., 1973. Positions des horizons dolomitiques mineralisés en fluorine et galène au sein des sediments triasíques de la Sierra de Lújar (Granada). Evolution et Geochimie. Thèse 3e cycle. Univ. Paris VI, pp. 166

Torres-Ruiz, J., Velilla, N., Martín, J.M., Delgado, F., Fenoll Hach-Ali, P., 1985. The fluorite-(Ba-Pb-Zn) Deposits of the “Sierra de Baza” (Betic Cordillera, South East Spain). Bull. Miner., Paris 108, 421–436.

Veizer, J., Ala, D., Azmy, K., Bruckschen, P., Buhl, D., Bruhn, F., Carden, G.A.F., Diener, A., Ebneth, S., Godderis, Y., Jasper, T., Korte, C., Pawellek, F., Podlaha, O.G., Strauss, H., 1999. , and evolution of Phanerozoic seawater. Chem. Geol. 161, 59–88. doi:10.1016/S0009-2541(99)00081-9

Velasco, F., Herrero, J.M., Gil, P.P., Alvarez, L., Yusta, I., 1994. Mississippi Valley type, Sedex and iron deposits in Lower Cretaceous rocks of the Basque-Cantabrian basin, northern Spain, in: Fontboté, L., Boni, M. (Eds.), Sediment-Hosted Zn-Pb Ores. Society of Geology Applied to Mineral Deposits Special Publication, pp. 246–270.

Vera, J.A., Arias, C., García-Hernández, M., López-Garrido, A.C., Martín-Algarra, A., Martín-Chivelet, J., Molina, J.M., Rivas, P., Ruiz-Ortiz, P.A., Sanz de Galdeano, C., Vilas, L., 2004. Las zonas externas béticas y el paelomargen sudibérico, in: Vera, J.A. (Ed.), Geología de España. Sociedad Geológica de España e Instituto Geológico de España, pp. 354–360.

Vergés, J., Fernàndez, M., 2012. Tethys-Atlantic interaction along the Iberia-Africa plate boundary: The Betic-Rif orogenic system. Tectonophysics 579, 144–172. doi:10.1016/j.tecto.2012.08.032

Vilas, L., Dabrio, C., Peláez, J.R., García-Hernández, M., 2001. Dominios sedimentarios generados durante el periodo extensional Cretácico Inferior entre Cazorla y Hellín (Béticas Externas). Su implicación en la estructural actual. Rev. la Soc. Geol. España 14, 113–122.

Williams, P.A., 1990. Oxide zone geochemistry. Ellis Horwood Ltd., London, pp. 286.

Figure captions:

Fig. 1. Geological map of the Betic Cordillera, southern Spain (modified from Vera et al., 2004), showing the location of the principal Zn-Pb-(F-Ag) ore districts (data obtained from Arribas and Tosdal, 1994; Delgado et al., 1971; Fenoll, 1987; Gervilla et al., 1985; Higueras et al., 1981; Manteca and Ovejero, 1992; Martín and Torres-Ruiz, 1982; Martin et al., 1987; Morales Ruano et al., 1995; Morales-Ruano et al., 1996; Oen et al., 1975; Ovejero et al., 1982; Tona, 1973; Torres-Ruiz et al., 1985).

Fig. 2. Geological map of the Riópar area with distribution and morphology of the hydrothermal dolomite (HTD) body and location of Zn-(Fe-Pb) ore deposits. Tr: Keuper Fm (Triassic clays and sandstones); Ji: Carretas to Contreras Fm (Lower Jurassic dolostones and limestones); Jm: Chorro Fm (Middle Jurassic dolostones); Js_2, Js_3, Ci_1: Sierra del Pozo Fm (Kimmeridgian to Hauterivian limestones and marls); Ci_2: Cerro Lobo Fm (Hauterivian to Valanginian marls and limestones); Ci_3: Arroyo de los Anchos Fm (Barremian to Aptian pisolitic and "callouix noire" limestones); Ci_4: Utrillas facies (Aptian to Albian sandstones and clays with dolomitized limestone levels); Cs_1, Cs_2, Cs_3: Dolomítica Fm (Cenomanian-Turonian dolostones); Cs_4: Sierra de la Solana Fm (Coniacian-Santonian limestones); Mc: Miocene polimictic conglomerate; Q_1: undifferentiated colluvium; Q_2: alluvial fans; Q_3: debris on alluvial funs; Q_4: recent colluvial; SF: Socovos fault; SJF: San Jorge fault; Sg1, Sg2: San Agustín deposits; Ro: Rosita deposit; Sj1, Sj2, Sj3: San Jorge deposits; Fc: Fuente de la Calentura mineralization.

Fig. 3. Cross sections (A and C) and detailed maps (B: San Agustín mine Sg2; and D: San Jorge mine Sj3) of the Zn-(Fe-Pb) mineralized zones. See Fig. 2 for location of cross sections, detailed maps and legend. The morphology of Zn-(Fe-Pb) ores has been deduced according to field observations and historic mining reports (Pellicio, 1845). St-HTD-Js_2: stratabound hydrothermal dolostone affecting Js_2 limestones; St-HTD-Ci_1: stratabound hydrothermal dolostone affecting Ci_1 limestones; Pt-HTD: patchy hydrothermal dolostone; SF: Socovos fault; SJF: San Jorge fault; 1) strata-concordant tabular Zn-(Fe-Pb) ore-bearing morphology; 2) strata-discordant tabular Zn-(Fe-Pb) ore-bearing morphology.

Fig. 4. (A) Outcrop photograph of cm-size sphalerite (Sph) vein. (B) Transmitted light (TL) microphotograph of sphalerite replacing planar-s (subhedral) replacive to planar-e (euhedral) sucrosic dolomite transition (ReD-SuD). (C) Hand sample photograph of sphalerite and saddle dolomite (SaD) cementing a ReD-SuD host-dolostone breccia. (D) TL photomicrograph showing fracture filling by early non-planar saddle dolomite (SaD-I), sphalerite and late non-planar saddle dolomite (SaD-II) hosted in ReD-SuD dolostone. (E) Detailed TL microphotograph of galena (Gn) associated with SaD-II. (F) Porphyrotopic dolomite replacing sphalerite crystals.

Fig. 5. Mine photographs of Zn-(Fe-Pb) non-sulfide ores. (A) Massive "red calamine" and "gossan" ores developed replacing Zn-(Fe-Pb) sulfide lenses. Zn-carbonates also occurs mixed with hydrothermal dolomites (HTD) and sphalerite (Sph). (B) Vein filled by "red calamine" mineralization with cockade textures that replace the Zn-(Fe-Pb) sulfide ore. (C) Massive "gossan" ore which replaces discordant sulfide lens. Gypsum is observed precipitating in the surface or filling porosity. (D) "Gossan" and "red

calamine" ores replacing stratiform Zn-(Fe-Pb) sulfide bodies (St: stratification; H-Carb: host-carbonate).

Fig. 6. (A) Hand sample photograph of smithsonite type-I (Sm-I) in veinlet crosscutting the host-dolostone (Host-Dol) showing a characteristic red-brown to orange colors with the application of Zinc Zap reactive. (B) Crustiform aspect of brown Sm-I. (C) Transmitted light (TL) microphotograph of Sm-I replacing partially a vein of sphalerite (Sph) hosted in replacive to sucrosic dolomite (ReD-SuD). (D) Cathodoluminescence (CL) image of Sm-I with bright to dull dark blue luminescence replacing sphalerite which post-date the non-planar saddle dolomite (SaD-I). (E) Smithsonite type-II (Sm-II) showing rugged appearance and brown colors. (F) TL microphotograph of Sm-II with Fe-(hydr)oxide bands replacing sphalerite and overgrowing posteriorly to Sm-I. (G) Secondary electron microscopy photograph of Sm-II showing platy shapes. (H) CL image of Sm-II with bright blue to pinkish luminescence.

Fig. 7. (A) White to grayish translucent smithsonite type-III (Sm-III) precipitated on saddle dolomite (SaD). (B) Transmitted under cross polarized light microphotograph of Sm-III precipitated on porosity whit botryoidal morphology and sweeping extinction. (C) Secondary electron microscopy photograph of Sm-III forming "rice grains". (D) Detailed microphotograph under SEM observation showing the platy shapes of the Sm-III. (E) Cathodoluminescence (CL) microphotograph of Sm-III with bright to dull dark blue luminescence with pink alternating bands. (F) White botryoidal hydrozincite (Hz) replacing smithsonite type-II (Sm-II) and precipitating on saddle dolomite (SaD).

Fig. 8. (A) Cathodoluminescence (CL) microphotograph of microcrystalline cerussite type-I (Cer-I) and type-II (Cer-II) associated with galena (Gn) and smithsonite type-I (Sm-I) and type-III (Sm-III) hosted in dolomite (Dol). (B) Reflected light (RL) microphotograph of Cer-I precipitated in galena crystal cleavage and Cer-II in porosity and fracture. (C) RL image of microcrystalline goethite type-I replacing marcasite (Mcs). (D) RL microphotograph of goethite type-II (Ght-II) forming plumose fans and partially replaced by botryoidal goethite type-III (Ght-III). (E) Transmitted light (TL) image of hematite (Hem) replacing marcasite. (F) Hand sample photograph of encrustation gypsum precipitated related to smithsonite type-III (Sm-III). (G) Brown calcite (BrC) along cleavage in saddle dolomite (SaD) and with calcite (WhC) infilling fractures and conforming brecciation. The pinkish to reddish color correspond to staining with alizarin red-s and potassium ferricyanide, which indicate that they are all non-ferroan. (H) Field observation of yellow calcite (YeC) druses in fracture zones.

Fig. 9. Wavelength Dispersion Spectrometry (WDS) microprobe profile analyses (ZnO, CaO, MgO, FeO and PbO) performed along three smithsonite type-III (Sm-III) crystals from center to border.

Fig. 10. $\delta^{13}C$ vs $\delta^{18}O$ cross-plot of host limestone (Host-Lim), replacive and sucrosic dolomite (ReD and SuD), saddle dolomite (SaD) related to sulfide Zn-(Fe-Pb) mineralization, smithsonite type-I (Sm-I), smithsonite type-II (Sm-II) and yellow calcite (YeC). Box indicates the range of Middle Jurassic to Lower Cretaceous marine carbonate according to Veizer et al. (1999). A C-O isotope comparison of smithsonite from other hypogene and supergene non-sulfide Zn deposits is also included.

Fig. 11. Histogram of S isotope data of sulfides and sulfate from Riópar deposit (Mcs: marcasite; Sph: sphalerite; Gn: galena; Gp: gypsum).

Fig. 12. Summary of the paragenetic sequence in the Riópar non-sulfide Zn-(Fe-Pb) ores and considering calcitization stage, as recognized from detailed conventional and cathodoluminescence petrography. The paragenetic sequence of the hypogene sulfides related to the hydrothermal dolomitization had been previously stablished by Navarro-Ciurana et al. (2016).

Fig. 13. Idealized geologic sketch of the Riópar non-sulfide Zn-(Fe-Pb) ore deposit and associated calcite and gypsum formation processes (SJF: San Jorge Fault). This evolution is very similar to that proposed by Choulet et al. (2014) and Reichert and Borg (2008) for the Zn non-sulfide ore deposits in Morocco and Iran.

Table captions:

Table 1. Relative mineral abundances in some representative samples of the Riópar Zn-(Fe-Pb) ores, as identified from X-ray diffraction (XRD) analyses and petrographic observations.

Table 2. Wavelength dispersive spectrometry (WDS) analyses of selected non-sulfide Zn-(Fe-Pb) phases from the Riópar area.

Table 3. C, O and S isotopic geochemistry of investigated phases.

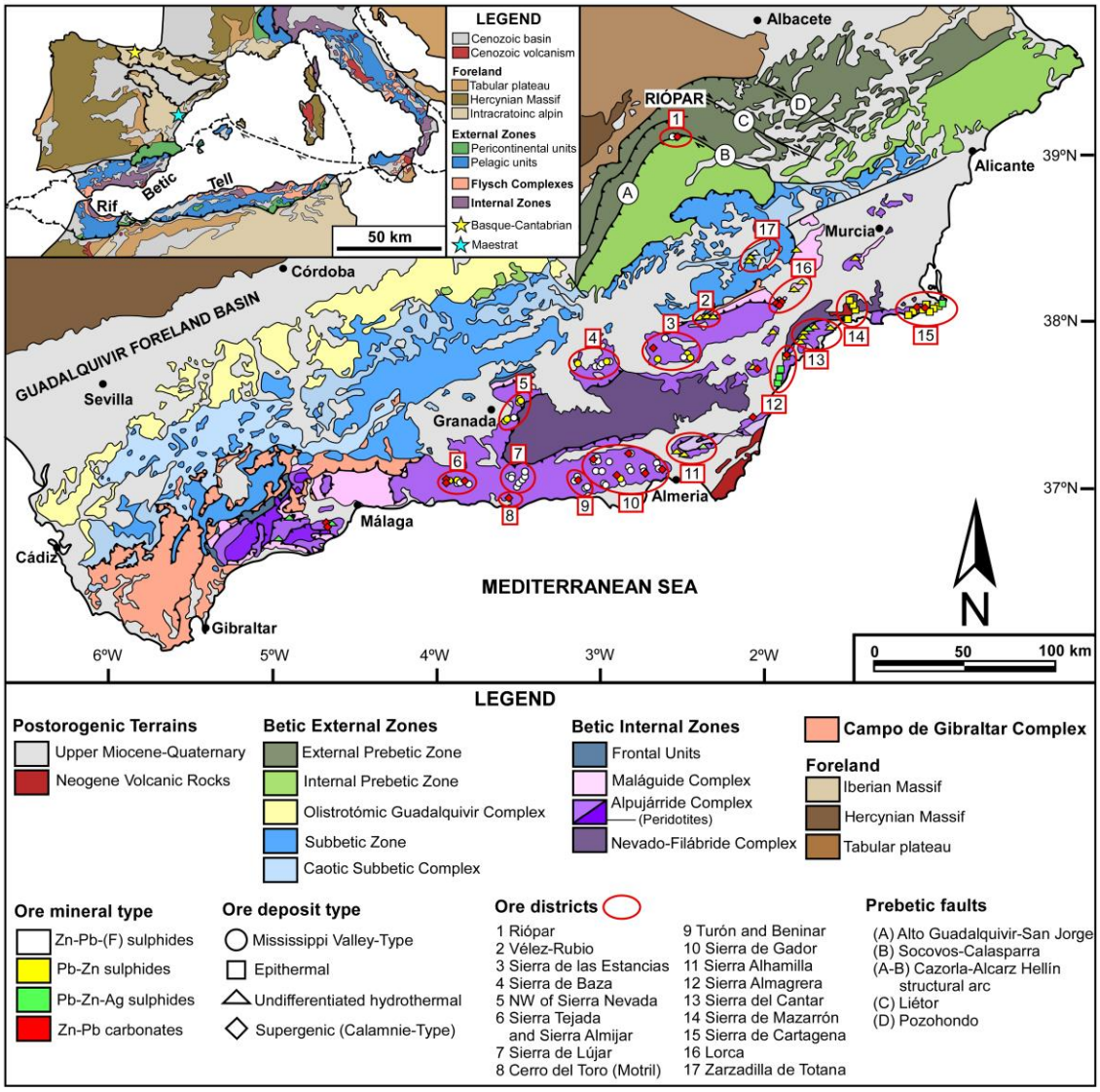
LEGEND
Cenozoic basin
Cenozoic volcanism
Foreland
Tabular plateau
Hercynian Massif
Intracratoinc alpin
External Zones
Pericontinental units
Pelagic units
Flysch Complexes
Internal Zones
Basque-Cantabrian
Maestrat
Rif
Betic
Tell
50 km
Albacete
RIÓPAR
Alicante
Murcia
Córdoba
GUADALQUIVIR FORELAND BASIN
Sevilla
Granada
Málaga
Almeria
Cádiz
Gibraltar
MEDITERRANEAN SEA
39ºN
38ºN
37ºN
6ºW
5ºW
4ºW
3ºW
2ºW
N
0
50
100 km
LEGEND
Postorogenic Terrains
Upper Miocene-Quaternary
Neogene Volcanic Rocks
Betic External Zones
External Prebetic Zone
Internal Prebetic Zone
Olistrotómic Guadalquivir Complex
Subbetic Zone
Caotic Subbetic Complex
Betic Internal Zones
Frontal Units
Maláguide Complex
Alpujárride Complex
(Peridotites)
Nevado-Filábride Complex
Campo de Gibraltar Complex
Foreland
Iberian Massif
Hercynian Massif
Tabular plateau
Ore mineral type
Zn-Pb-(F) sulphides
Pb-Zn sulphides
Pb-Zn-Ag sulphides
Zn-Pb carbonates
Ore deposit type
Mississippi Valley-Type
Epithermal
Undifferentiated hydrothermal
Supergenic (Calamnie-Type)
Ore districts
1 Riópar
2 Vélez-Rubio
3 Sierra de las Estancias
4 Sierra de Baza
5 NW of Sierra Nevada
6 Sierra Tejada and Sierra Almijar
7 Sierra de Lújar
8 Cerro del Toro (Motril)
9 Turón and Beninar
10 Sierra de Gador
11 Sierra Alhamilla
12 Sierra Almagrera
13 Sierra del Cantar
14 Sierra de Mazarrón
15 Sierra de Cartagena
16 Lorca
17 Zarzadilla de Totana
Prebetic faults
(A) Alto Guadalquivir-San Jorge
(B) Socovos-Calasparra
(A-B) Cazorla-Alcarz Hellín structural arc
(C) Liétor
(D) Pozohondo

Figure 1

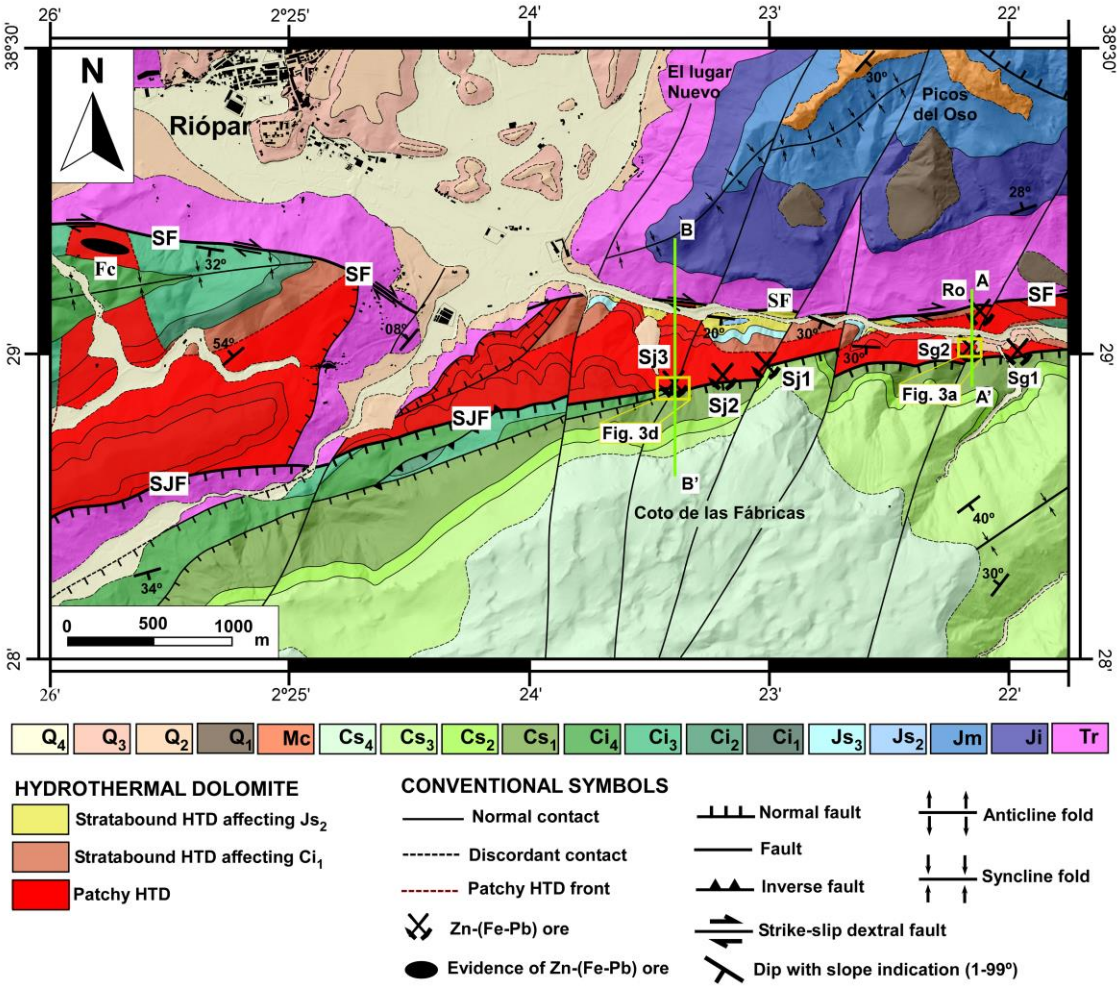
26'
2°25'
24'
23'
22'
38°30'
29'
28'
N
Riópar
El lugar Nuevo
Picos del Oso
SF
Fc
SJF
Sj1
Sj2
Sj3
Sg1
Sg2
Ro
A
A'
B
B'
Fig. 3a
Fig. 3d
Coto de las Fábricas
0 500 1000 m
Q4 Q3 Q2 Q1 Mc Cs4 Cs3 Cs2 Cs1 Ci4 Ci3 Ci2 Ci1 Js3 Js2 Jm Ji Tr
HYDROTHERMAL DOLOMITE
Stratabound HTD affecting Js2
Stratabound HTD affecting Ci1
Patchy HTD
CONVENTIONAL SYMBOLS
Normal contact
Discordant contact
Patchy HTD front
Zn-(Fe-Pb) ore
Evidence of Zn-(Fe-Pb) ore
Normal fault
Fault
Inverse fault
Strike-slip dextral fault
Dip with slope indication (1-99°)
Anticline fold
Syncline fold

Figure 2

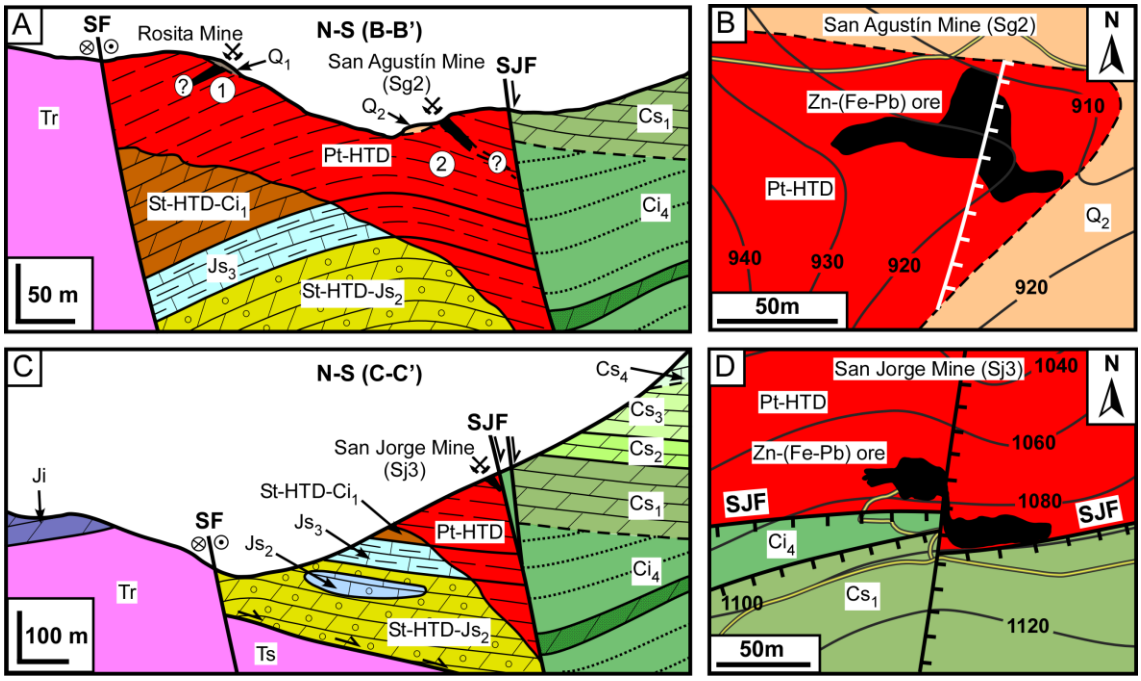
A
SF
Rosita Mine
N-S (B-B')
Q1
San Agustín Mine
(Sg2)
SJF
Q2
Tr
Cs1
Pt-HTD
St-HTD-Ci1
Ci4
Js3
St-HTD-Js2
50 m
B
San Agustín Mine (Sg2)
N
Zn-(Fe-Pb) ore
910
Pt-HTD
Q2
940
930
920
920
50m
C
N-S (C-C')
Cs4
Cs3
SJF
Cs2
San Jorge Mine
(Sj3)
Ji
St-HTD-Ci1
Cs1
SF
Js3
Js2
Pt-HTD
Ci4
Tr
St-HTD-Js2
100 m
Ts
D
San Jorge Mine (Sj3)
1040
N
Pt-HTD
1060
Zn-(Fe-Pb) ore
SJF
1080
SJF
Ci4
Cs1
1100
1120
50m

Figure 3

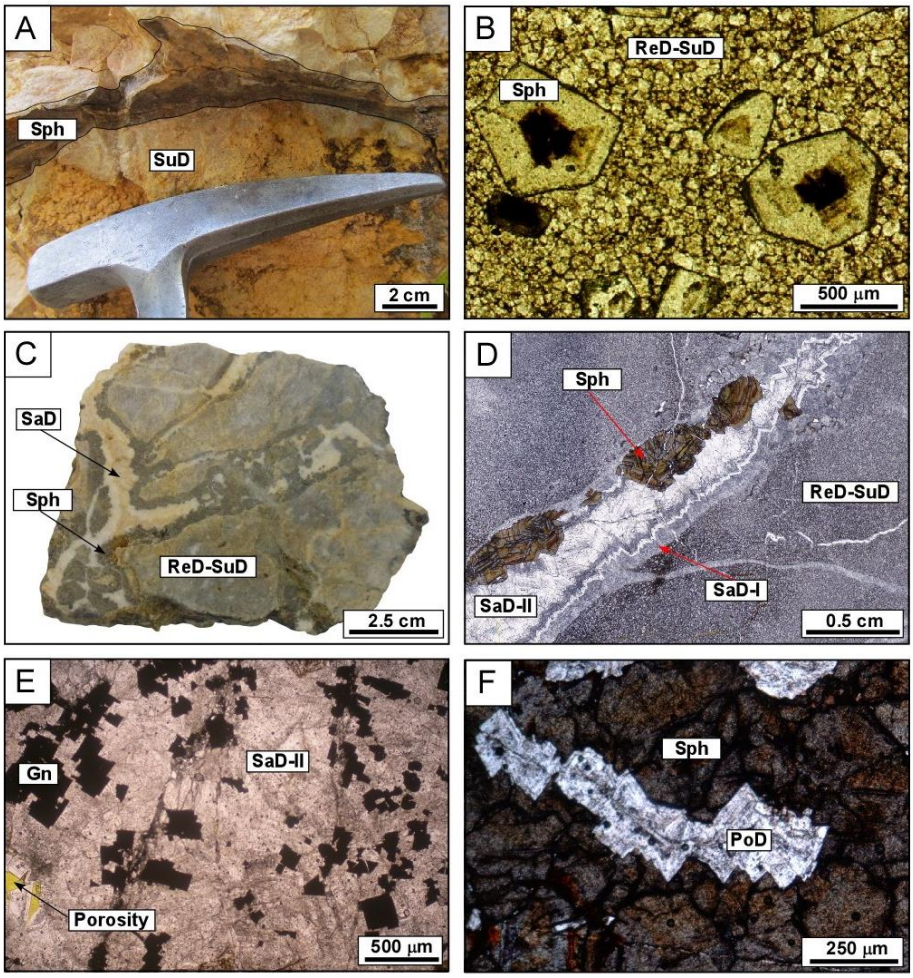
A
Sph
SuD
2 cm
B
ReD-SuD
Sph
500 µm
C
SaD
Sph
ReD-SuD
2.5 cm
D
Sph
ReD-SuD
SaD-II
SaD-I
0.5 cm
E
Gn
SaD-II
Porosity
500 µm
F
Sph
PoD
250 µm

Figure 4

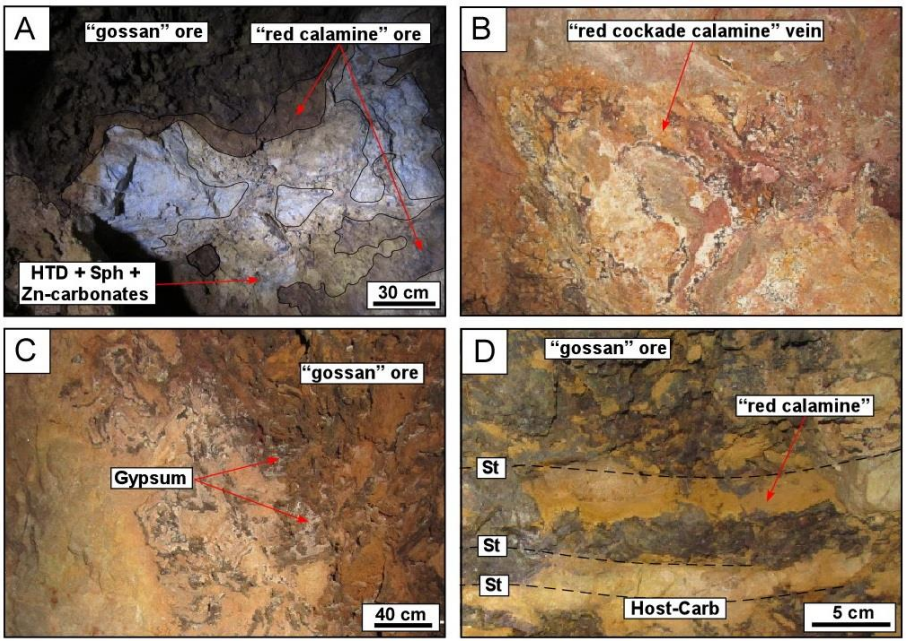
A
"gossan" ore
"red calamine" ore
HTD + Sph +
Zn-carbonates
30 cm
B
"red cockade calamine" vein
C
"gossan" ore
Gypsum
40 cm
D
"gossan" ore
"red calamine"
St
St
St
Host-Carb
5 cm

Figure 5

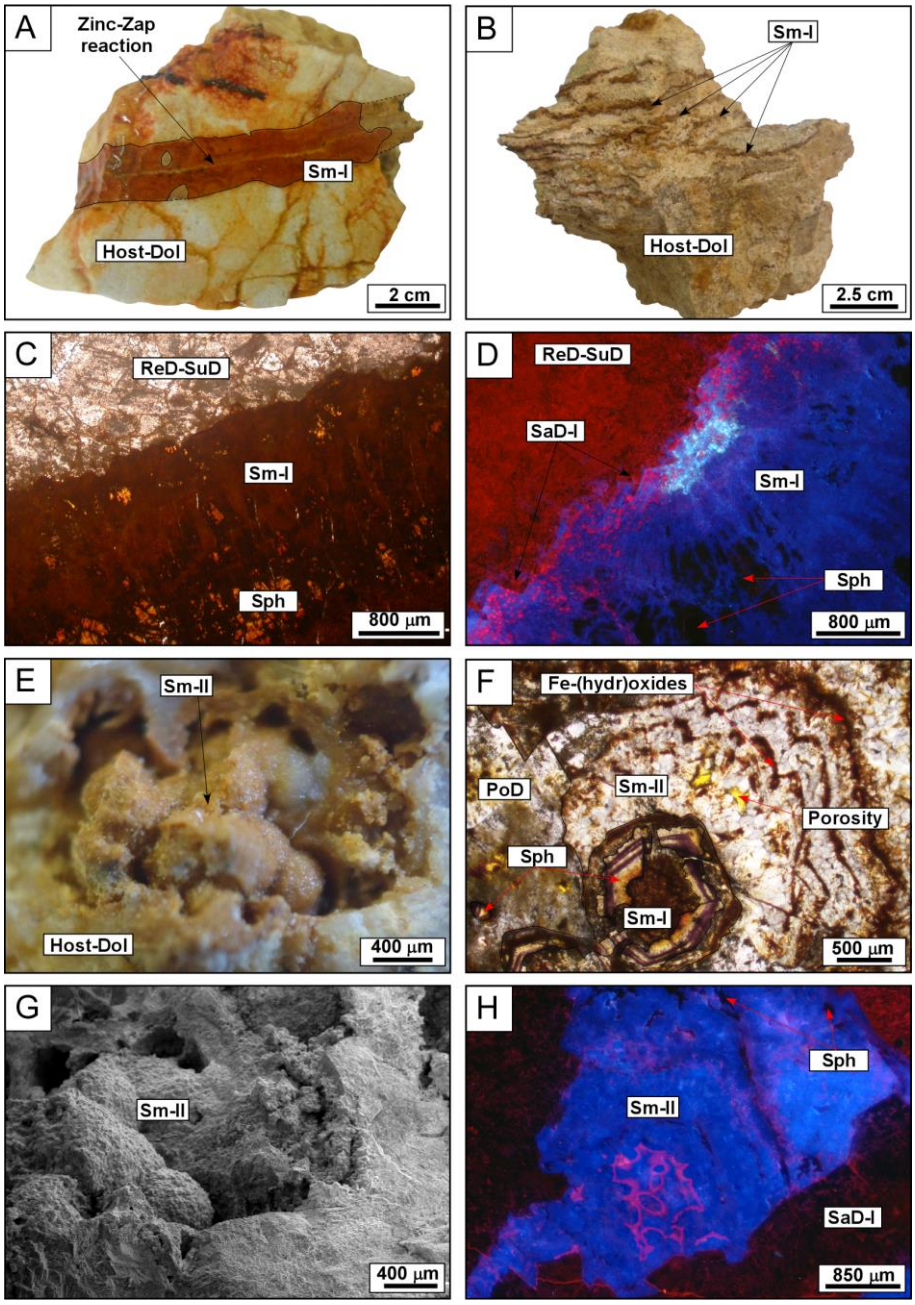
A
Zinc-Zap reaction
Sm-I
Host-Dol
2 cm
B
Sm-I
Host-Dol
2.5 cm
C
ReD-SuD
Sm-I
Sph
800 µm
D
ReD-SuD
SaD-I
Sm-I
Sph
800 µm
E
Sm-II
Host-Dol
400 µm
F
Fe-(hydr)oxides
PoD
Sm-II
Porosity
Sph
Sm-I
500 µm
G
Sm-II
400 µm
H
Sph
Sm-II
SaD-I
850 µm

Figure 6

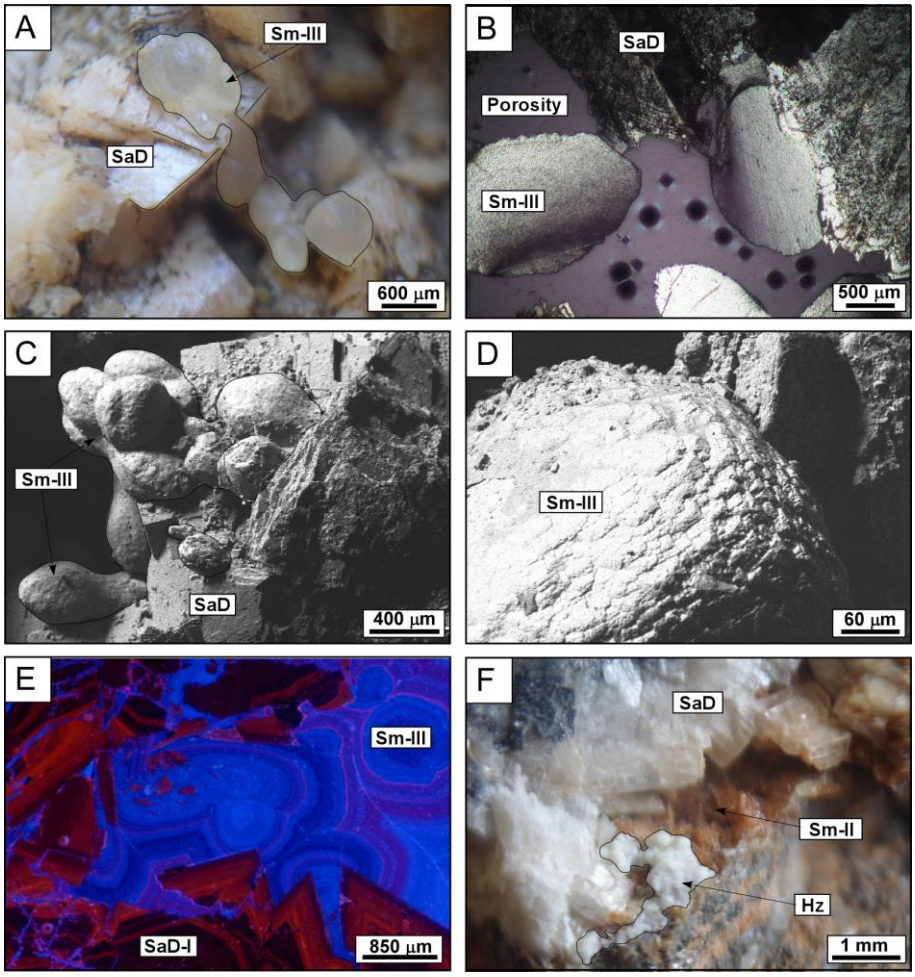
A
Sm-III
SaD
600 µm
B
SaD
Porosity
Sm-III
500 µm
C
Sm-III
SaD
400 µm
D
Sm-III
60 µm
E
Sm-III
SaD-I
850 µm
F
SaD
Sm-II
Hz
1 mm

Figure 7

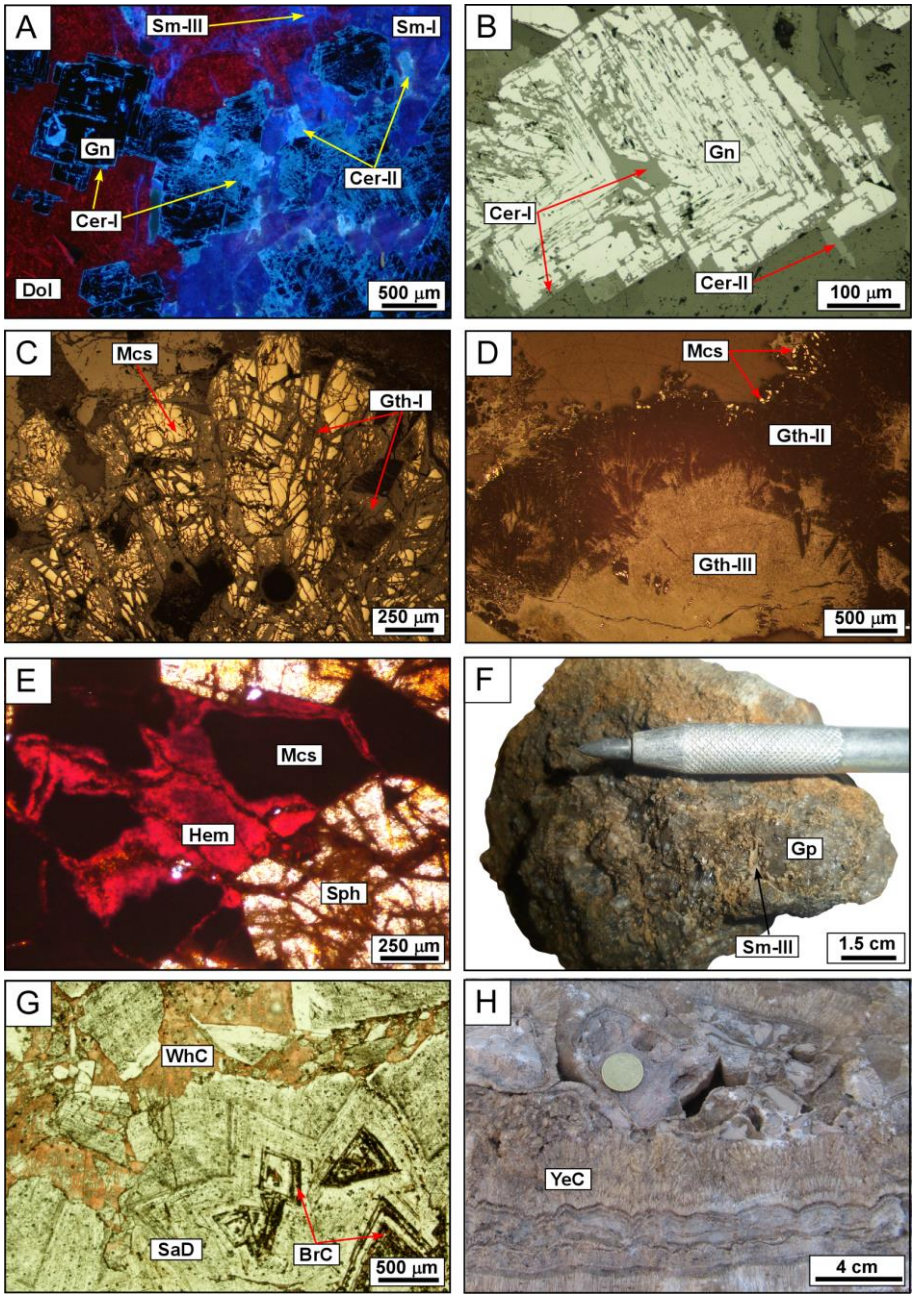
A
Sm-III
Sm-I
Gn
Cer-II
Cer-I
Dol
500 µm
B
Gn
Cer-I
Cer-II
100 µm
C
Mcs
Gth-I
250 µm
D
Mcs
Gth-II
Gth-III
500 µm
E
Mcs
Hem
Sph
250 µm
F
Gp
Sm-III
1.5 cm
G
WhC
SaD
BrC
500 µm
H
YeC
4 cm

Figure 8

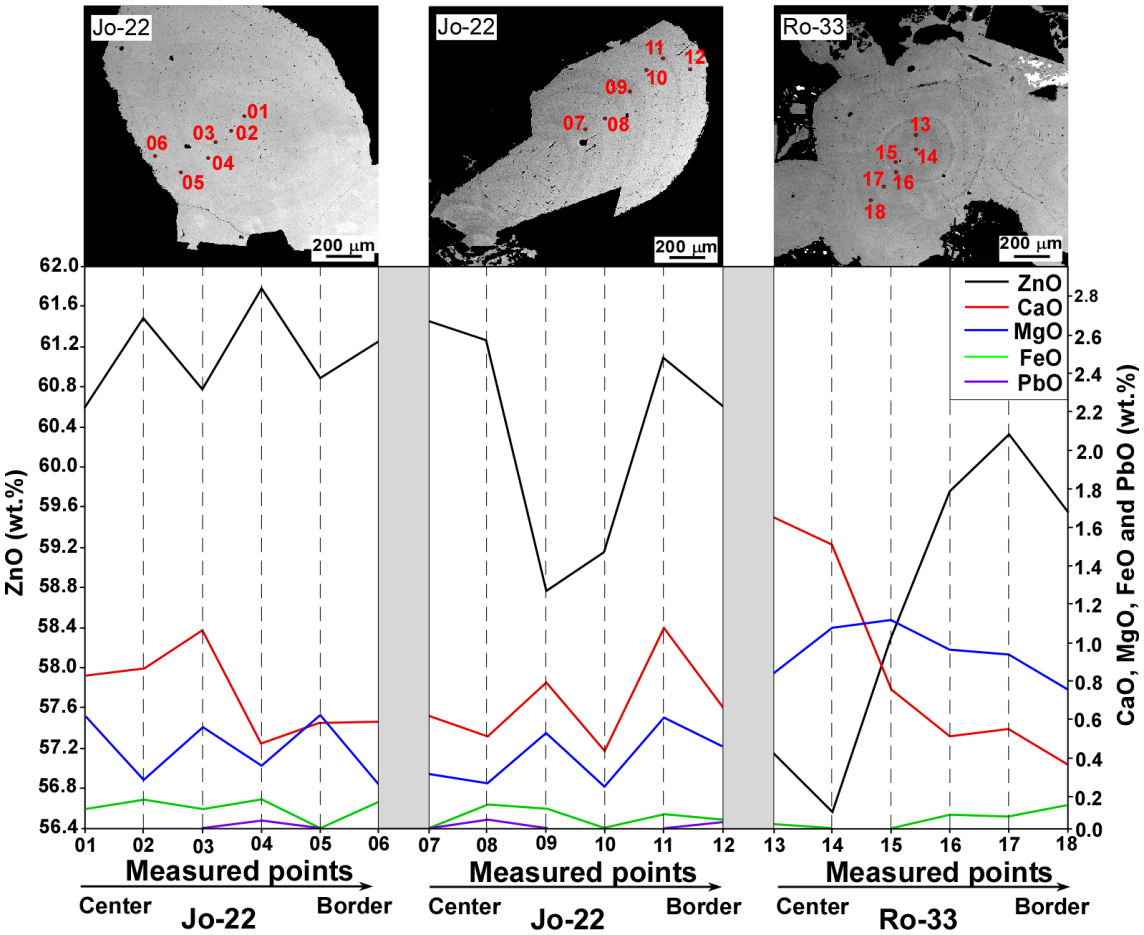
Jo-22
Jo-22
Ro-33
200 µm
ZnO
CaO
MgO
FeO
PbO
ZnO (wt.%)
CaO, MgO, FeO and PbO (wt.%)
Measured points
Center
Jo-22
Border
Ro-33

Figure 9

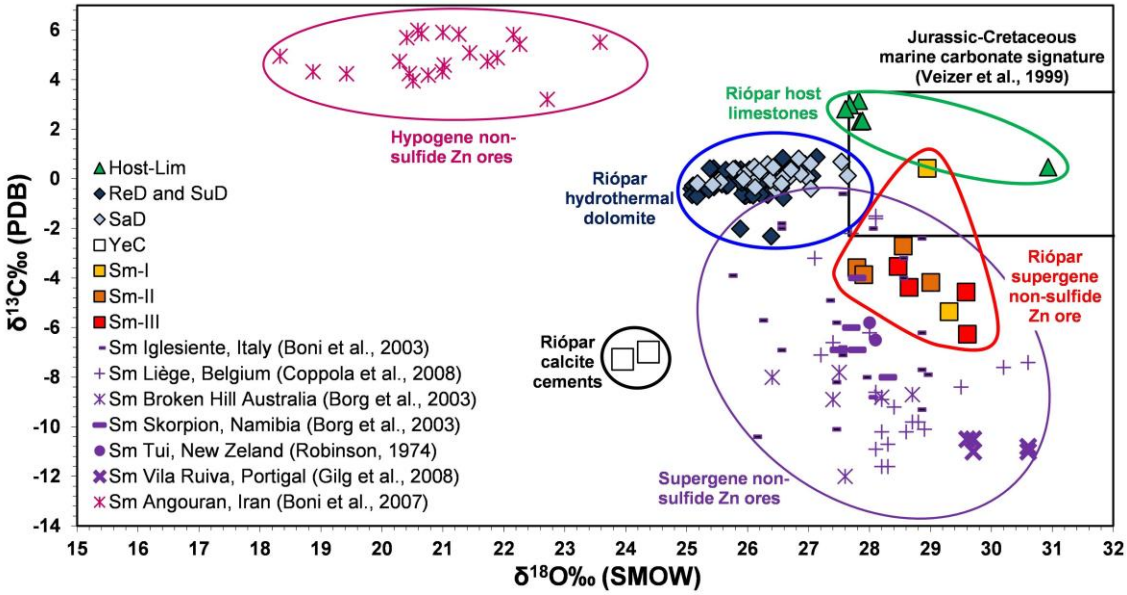
Jurassic-Cretaceous marine carbonate signature (Veizer et al., 1999)
Riópar host limestones
Hypogene non-sulfide Zn ores
Riópar hydrothermal dolomite
Riópar supergene non-sulfide Zn ore
Riópar calcite cements
Supergene non-sulfide Zn ores
Host-Lim
ReD and SuD
SaD
YeC
Sm-I
Sm-II
Sm-III
Sm Iglesiente, Italy (Boni et al., 2003)
Sm Liège, Belgium (Coppola et al., 2008)
Sm Broken Hill Australia (Borg et al., 2003)
Sm Skorpion, Namibia (Borg et al., 2003)
Sm Tui, New Zeland (Robinson, 1974)
Sm Vila Ruiva, Portigal (Gilg et al., 2008)
Sm Angouran, Iran (Boni et al., 2007)
δ13C‰ (PDB)
δ18O‰ (SMOW)

Figure 10

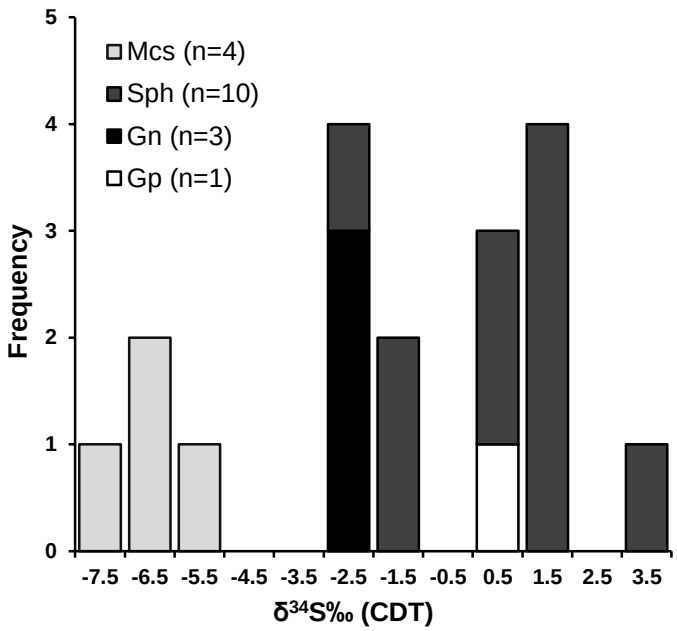
Mcs (n=4)
Sph (n=10)
Gn (n=3)
Gp (n=1)
Frequency
0
1
2
3
4
5
-7.5
-6.5
-5.5
-4.5
-3.5
-2.5
-1.5
-0.5
0.5
1.5
2.5
3.5
δ34S‰ (CDT)

Figure 11

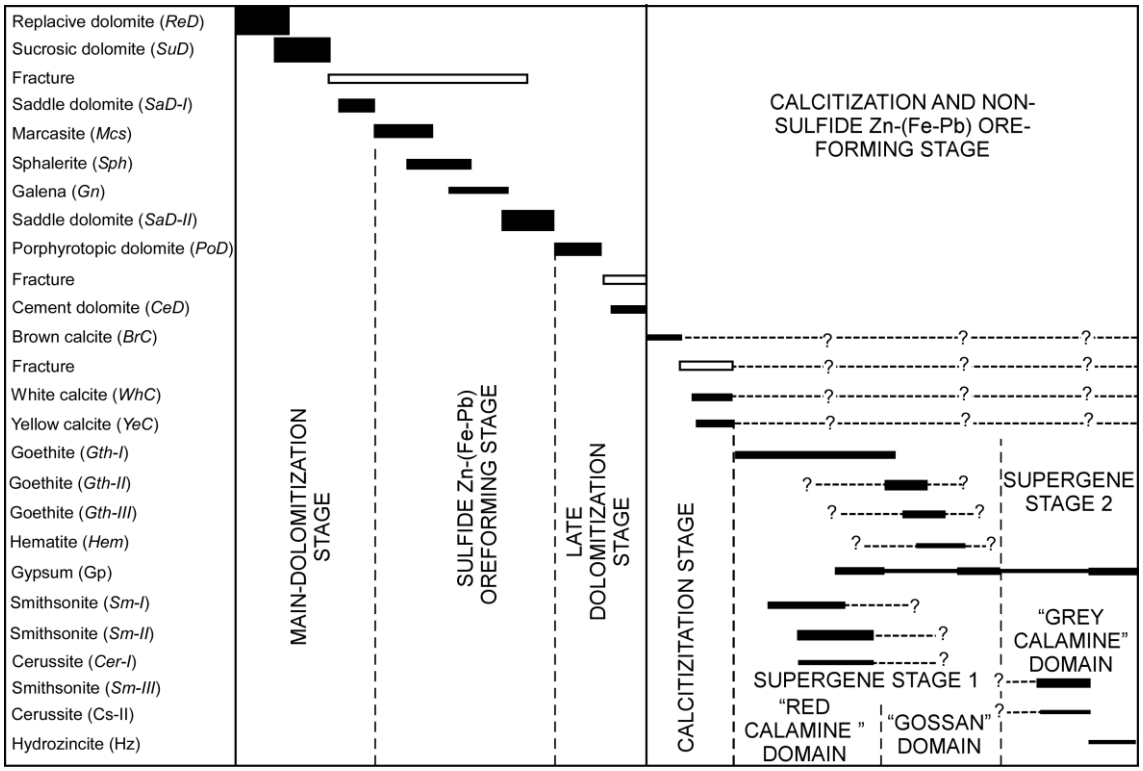
Replacive dolomite (ReD)
Sucrosic dolomite (SuD)
Fracture
Saddle dolomite (SaD-I)
Marcasite (Mcs)
Sphalerite (Sph)
Galena (Gn)
Saddle dolomite (SaD-II)
Porphyrotopic dolomite (PoD)
Fracture
Cement dolomite (CeD)
Brown calcite (BrC)
Fracture
White calcite (WhC)
Yellow calcite (YeC)
Goethite (Gth-I)
Goethite (Gth-II)
Goethite (Gth-III)
Hematite (Hem)
Gypsum (Gp)
Smithsonite (Sm-I)
Smithsonite (Sm-II)
Cerussite (Cer-I)
Smithsonite (Sm-III)
Cerussite (Cs-II)
Hydrozincite (Hz)
MAIN-DOLOMITIZATION STAGE
SULFIDE Zn-(Fe-Pb) OREFORMING STAGE
LATE DOLOMITIZATION STAGE
CALCITIZITATION STAGE
CALCITIZATION AND NON-SULFIDE Zn-(Fe-Pb) ORE-FORMING STAGE
SUPERGENE STAGE 2
"GREY CALAMINE" DOMAIN
SUPERGENE STAGE 1
"RED CALAMINE " DOMAIN
"GOSSAN" DOMAIN

Figure 12

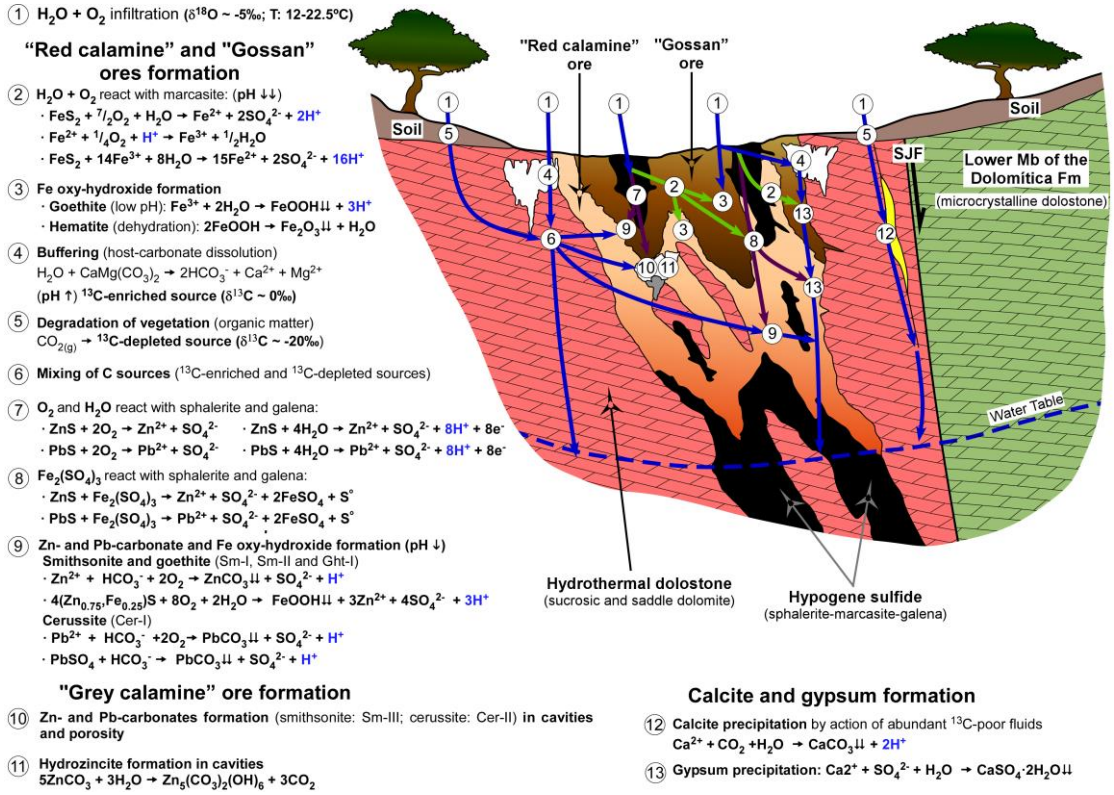
① $H_2O + O_2$ infiltration ($\delta^{18}O$ ~ -5‰; T: 12-22.5ºC)
"Red calamine" and "Gossan" ores formation
② $H_2O + O_2$ react with marcasite: (pH ↓↓)
· $FeS_2 + {}^7/_2O_2 + H_2O \rightarrow Fe^{2+} + 2SO_4^{2-} + 2H^+$
· $Fe^{2+} + {}^1/_4O_2 + H^+ \rightarrow Fe^{3+} + {}^1/_2H_2O$
· $FeS_2 + 14Fe^{3+} + 8H_2O \rightarrow 15Fe^{2+} + 2SO_4^{2-} + 16H^+$
③ Fe oxy-hydroxide formation
· Goethite (low pH): $Fe^{3+} + 2H_2O \rightarrow FeOOH\downarrow\downarrow + 3H^+$
· Hematite (dehydration): $2FeOOH \rightarrow Fe_2O_3\downarrow\downarrow + H_2O$
④ Buffering (host-carbonate dissolution)
$H_2O + CaMg(CO_3)_2 \rightarrow 2HCO_3^- + Ca^{2+} + Mg^{2+}$
(pH ↑) ^{13}C-enriched source ($\delta^{13}C$ ~ 0‰)
⑤ Degradation of vegetation (organic matter)
$CO_{2(g)} \rightarrow$ ^{13}C-depleted source ($\delta^{13}C$ ~ -20‰)
⑥ Mixing of C sources (^{13}C-enriched and ^{13}C-depleted sources)
⑦ O_2 and H_2O react with sphalerite and galena:
· $ZnS + 2O_2 \rightarrow Zn^{2+} + SO_4^{2-}$ · $ZnS + 4H_2O \rightarrow Zn^{2+} + SO_4^{2-} + 8H^+ + 8e^-$
· $PbS + 2O_2 \rightarrow Pb^{2+} + SO_4^{2-}$ · $PbS + 4H_2O \rightarrow Pb^{2+} + SO_4^{2-} + 8H^+ + 8e^-$
⑧ $Fe_2(SO_4)_3$ react with sphalerite and galena:
· $ZnS + Fe_2(SO_4)_3 \rightarrow Zn^{2+} + SO_4^{2-} + 2FeSO_4 + S^\circ$
· $PbS + Fe_2(SO_4)_3 \rightarrow Pb^{2+} + SO_4^{2-} + 2FeSO_4 + S^\circ$
⑨ Zn- and Pb-carbonate and Fe oxy-hydroxide formation (pH ↓)
Smithsonite and goethite (Sm-I, Sm-II and Ght-I)
· $Zn^{2+} + HCO_3^- + 2O_2 \rightarrow ZnCO_3\downarrow\downarrow + SO_4^{2-} + H^+$
· $4(Zn_{0.75},Fe_{0.25})S + 8O_2 + 2H_2O \rightarrow FeOOH\downarrow\downarrow + 3Zn^{2+} + 4SO_4^{2-} + 3H^+$
Cerussite (Cer-I)
· $Pb^{2+} + HCO_3^- + 2O_2 \rightarrow PbCO_3\downarrow\downarrow + SO_4^{2-} + H^+$
· $PbSO_4 + HCO_3^- \rightarrow PbCO_3\downarrow\downarrow + SO_4^{2-} + H^+$
"Red calamine" ore
"Gossan" ore
Soil
Soil
SJF
Lower Mb of the Dolomitica Fm
(microcrystalline dolostone)
Water Table
Hydrothermal dolostone
(sucrosic and saddle dolomite)
Hypogene sulfide
(sphalerite-marcasite-galena)
"Grey calamine" ore formation
⑩ Zn- and Pb-carbonates formation (smithsonite: Sm-III; cerussite: Cer-II) in cavities and porosity
⑪ Hydrozincite formation in cavities
$5ZnCO_3 + 3H_2O \rightarrow Zn_5(CO_3)_2(OH)_6 + 3CO_2$
Calcite and gypsum formation
⑫ Calcite precipitation by action of abundant ^{13}C-poor fluids
$Ca^{2+} + CO_2 + H_2O \rightarrow CaCO_3\downarrow\downarrow + 2H^+$
⑬ Gypsum precipitation: $Ca2^+ + SO_4^{2-} + H_2O \rightarrow CaSO_4{\cdot}2H_2O\downarrow\downarrow$

Figure 13

TABLE 1

Sample	Location	Coordinates (ºWGS-84)		Dol	Sph	Mcs	Gn	Sm	Hz	Gth	Cer	Cal	Gp
		Latitude	Longitude										
Jo-20a	San Jorge	-2.384339	38.482719	+++	+	+	+	+	n.f.	n.f.	+	n.f.	n.f.
Jo-20f	San Jorge	-2.384339	38.482719	++	+	+	+	+++	n.f.	+	+	n.f.	n.f.
Jo-22	San Jorge	-2.392451	38.485325	+++	+	n.f.	n.f.	++	n.f.	n.f.	n.f.	n.f.	n.f.
Sj-31	San Jorge	-2.383959	38.482198	+++	n.f.	n.f.	n.f.	++	n.f	n.f.	n.f.	n.f.	n.f.
Sj-33	San Jorge	-2.383959	38.482198	+++	++	+	n.f.	+	n.f.	++	+	++	+
Sj-40b	San Jorge	-2.383959	38.482198	+++	n.f.	n.f.	n.f.	++	+	+	+	n.f	n.f.
Ro-03	San Agustín	-2.369360	38.483357	+++	+	n.f.	n.f.	++	n.f.	n.f.	+	n.f.	n.f.
Sg-04a	San Agustín	-2.366550	38.482815	+++	n.f.	n.f.	n.f.	++	n.f.	n.f.	n.f.	n.f.	n.f.

Mineral abbreviations: Dol, dolomite; Sph, sphalerite; Mcs, marcasite; Gn, galena; Sm, smithsonite; Hz, hydrozincite; Cer, cerussite; Gth, goethite; Cal, calcite; Gp: gypsum
High abundance (+++); moderate abundance (++); low abundance (+); not found (n.f.)

TABLE 2

Phase[(a)]	ZnO	CaO	MgO	FeO	PbO	SrO	BaO	MnO	Na_2O	Total	Zn	Ca	Mg	Fe	Pb	Sr	Ba	Mn	Na
	(wt.%)										atoms per formula unit (a.p.f.u.)								
Sm-I																			
n	3	3	3	3	3	3	1	2	-	3	3	3	3	3	3	3	1	2	-
Min.	56.18	0.70	0.20	0.01	0.76	0.10	-	0.01	-	62.14	0.904	0.010	0.002	0.000	0.014	0.002	-	0.000	-
Mean	58.92	0.71	0.35	1.20	0.99	0.17	0.03	0.04	-	62.35	0.945	0.010	0.004	0.019	0.018	0.003	0.001	0.000	-
Max.	60.67	0.72	0.58	3.52	1.44	0.22	-	0.07	-	62.65	0.969	0.010	0.007	0.055	0.027	0.004	-	0.001	-
St. dv.	2.40	0.01	0.20	2.01	0.39	0.06	-	0.04	-	0.27	0.036	0.000	0.002	0.031	0.007	0.001	-	0.000	-
Sm-II									-										
n	24	24	24	24	22	23	-	5	-	24	24	24	24	24	22	23	-	5	-
Min.	60.20	0.26	0.26	0.01	0.04	0.03	-	0.01	-	64.02	0.934	0.004	0.005	0.000	0.000	0.000	-	0.000	-
Mean	63.57	0.60	0.60	0.29	0.13	0.16	-	0.01	-	65.52	0.973	0.008	0.009	0.004	0.002	0.003	-	0.000	-
Max.	68.71	1.30	1.30	3.13	0.26	0.29	-	0.03	-	70.67	0.983	0.018	0.018	0.047	0.005	0.005	-	0.000	-
St. dv.	1.52	0.40	0.40	0.64	0.06	0.06	-	0.01	-	1.35	0.010	0.005	0.003	0.010	0.001	0.001	-	0.000	-
Sm-III																			
n	18	18	18	7	9	18	8	8	-	18	18	18	18	7	9	18	8	8	-
Min.	56.74	0.33	0.21	0.02	0.04	0.11	0.05	0.01	-	59.55	0.959	0.005	0.003	0.000	0.000	0.002	0.000	0.000	-
Mean	60.10	0.72	0.56	0.05	0.11	0.19	0.10	0.03	-	61.71	0.977	0.010	0.007	0.001	0.002	0.003	0.002	0.001	-
Max.	61.77	1.62	1.08	0.12	0.15	0.24	0.19	0.11	-	63.01	0.987	0.024	0.014	0.002	0.003	0.004	0.003	0.002	-
St. dv.	1.46	0.36	0.29	0.03	0.04	0.04	0.05	0.03	-	1.13	0.008	0.005	0.004	0.001	0.001	0.001	0.001	0.001	-
Cer-I																			
n	2	2	-	-	2	2	2	-	-	2	2	2	-	-	2	2	2	-	-
Min.	0.01	0.06	-	-	82.07	0.78	0.06	-	-	83.21	-	0.001	-	-	0.988	0.008	0.001	-	-
Mean	0.01	0.17	-	-	82.48	0.79	0.08	-	-	83.55	0.000	0.002	-	-	0.989	0.009	0.001	-	-
Max.	0.01	0.29	-	-	82.88	0.81	0.10	-	-	83.88	-	0.003	-	-	0.989	0.009	0.001	-	-
St. dv.	0.00	0.17	-	-	0.57	0.02	0.03	-	-	0.47	-	0.002	-	-	0.001	0.000	0.000	-	-
Ght-I																			
n	3	3	3	3	2	2	2	-	1	3	3	3	3	3	2	2	2	-	1
Min.	2.25	0.04	0.05	63.96	1.44	0.04	0.02	-	-	71.57	0.029	0.000	0.000	0.888	0.024	0.001	0.000	-	-
Mean	4.14	0.09	0.06	71.05	2.31	0.09	0.03	-	0.23	77.04	0.056	0.001	0.001	0.917	0.035	0.001	0.000	-	0.000
Max.	6.02	0.15	0.09	76.42	3.19	0.14	0.04	-	-	80.41	0.086	0.002	0.001	0.965	0.047	0.002	0.001	-	-
St. dv.	1.88	0.06	0.02	6.41	1.24	0.07	0.01	-	-	4.78	0.029	0.001	0.000	0.042	0.016	0.001	0.000	-	-
Ght-II																			
n	5	5	3	5	-	5	1	-	4	5	5	5	3	5	-	5	1	-	4
Min.	0.73	0.03	0.04	71.78	-	0.05	-	-	0.14	74.34	0.005	0.000	0.000	0.966	-	0.001	-	-	0.001
Mean	1.50	0.05	0.05	76.07	-	0.12	0.03	-	0.18	77.92	0.019	0.001	0.000	0.977	-	0.002	0.000	-	0.001
Max.	2.07	0.08	0.05	78.40	-	0.20	-	-	0.22	80.62	0.029	0.001	0.001	0.987	-	0.003	-	-	0.001
St. dv.	0.57	0.02	0.01	2.59	-	0.06	-	-	0.08	2.48	0.009	0.000	0.000	0.009	-	0.001	-	-	0.000
Ght-III																			
n	3	3	2	3	-	3	3	-	3	3	3	3	2	3	-	3	3	-	3
Min.	2.26	0.02	0.03	72.91	-	0.07	0.04	-	0.25	77.21	0.030	0.000	-	0.943	-	0.001	0.001	-	0.002
Mean	3.30	008	0.04	74.16	-	0.08	0.10	-	0.31	78.03	0.044	0.001	0.000	0.951	-	0.001	0.001	-	0.002
Max.	3.95	0.14	0.05	74.85	-	0.08	0.15	-	0.34	79.42	0.051	0.002	-	0.965	-	0.001	0.002	-	0.002
St. dv.	0.91	0.06	0.02	1.08	-	0.01	0.05	-	0.05	1.21	0.012	0.001	-	0.012	-	0.000	0.001	-	0.000

[(a)] Sm-I: smithsonite type-I; Sm-II: smithsonite type II; Sm-III: smithsonite type-III; Cer-I: cerussite type-I; Ght-I: goethite type-I; Ght-II: goethite type-II; Ght-III: goethite type-III; n: number of analyses; min.: minimum value; mean: mean value; max.: maximum value; St. dv.: Standard deviation.

TABLE 3

Phase[(a)]	$\delta^{13}C$ (‰ PDB)	$\delta^{18}O$ (‰ SMOW)	$\delta^{34}S$ (‰ CDT)
Host-lim			
n	6	6	-
Min.	+0.5	+27.6	-
Mean	+2.3	+28.3	-
Max.	+3.2	+30.9	-
St. dv.	1.0	1.3	-
ReD-SuD			
n	65	65	-
Min.	-2.3	+25.1	-
Mean	-0.2	+26.0	-
Max.	+0.9	+27.1	-
St. dv.	0.6	0.5	-
SaD			
n	32	32	-
Min.	-0.4	+25.2	-
Mean	+0.1	+26.4	-
Max.	+0.8	+27.6	-
St. dv.	0.3	0.6	-
Sm-I			
n	2	2	-
Min.	-5.4	+28.9	-
Mean	-2.5	+29.1	-
Max.	+0.4	+29.3	-
St. dv.	4.1	0.3	-
Sm-II			
n	4	4	-
Min.	-4.1	+27.8	-
Mean	-3.6	+28.3	-
Max.	-2.7	+29.0	-
St. dv.	0.6	0.6	-
Sm-III			
n	4	4	-
Min.	-6.3	+28.5	-
Mean	-4.7	+29.1	-
Max.	-3.5	+29.6	-
St. dv.	1.1	0.6	-
YeC			
n	2	2	-
Min.	-7.3	+23.9	-
Mean	-7.1	+24.2	-
Max.	-7.0	+24.4	-
St. dv.	0.2	0.3	-
Mcs			
n	-	-	4
Min.	-	-	-7.5
Mean	-	-	-6.6
Max.	-	-	-5.8
St. dv.	-	-	0.8
Sph			
n	-	-	10
Min.	-	-	-2.2
Mean	-	-	+0.5
Max.	-	-	+3.5
St. dv.	-	-	1.8
Gn			
n	-	-	3
Min.	-	-	-2.8
Mean	-	-	-2.6
Max.	-	-	-2.4
St. dv.	-	-	0.2
Gp			
n	-	-	1
Mean	-	-	+0.1

Host-lim: host-limestone; ReD-SuD: replacive and sucrosic dolomite; SaD: saddle dolomite; Sm-I: smithsonite type-I; Sm-II: smithsonite type-II; Sm-III: smithsonite type-III; YeC: yellow calcite; Mcs: marcasite; Sph: sphalerite; Gn: galena; Gp: gypsum; n: number of analyses; min.: minimum value; mean: mean value; max.: maximum value; St. dv.: Standard deviation.